TRINIDI: Time-of-Flight Resonance Imaging With Neutrons for Isotopic Density Inference

Thilo Balke, *Member, IEEE*, Alexander M. Long, Sven C. Vogel, Brendt Wohlberg, *Fellow, IEEE*, and Charles A. Bouman, *Life Fellow, IEEE*

***Abstract*—Accurate reconstruction of 2D and 3D isotope densities is a desired capability with great potential impact in applications such as evaluation and development of next-generation nuclear fuels. Neutron time-of-flight (TOF) resonance imaging offers a potential approach by exploiting the characteristic neutron absorption spectra of each isotope. However, it is a major challenge to compute quantitatively accurate images due to a variety of confounding effects such as severe Poisson noise, background scatter, beam non-uniformity, absorption non-linearity, and extended source pulse duration. We present the TRINIDI algorithm which is based on a two-step process in which we first estimate the neutron flux and background counts, and then reconstruct the areal densities of each isotope and pixel. Both components are based on the inversion of a forward model that accounts for the highly non-linear absorption, energy-dependent emission profile, and Poisson noise, while also modeling the substantial spatio-temporal variation of the background and flux. To do this, we formulate the non-linear inverse problem as two optimization problems that are solved in sequence. We demonstrate on both synthetic and measured data that TRINIDI can reconstruct quantitatively accurate 2D views of isotopic areal density that can then be reconstructed into quantitatively accurate 3D volumes of isotopic volumetric density.**

***Index Terms*—Neutron resonance imaging, time-of-flight, tomography, material decomposition, isotope density, poisson noise, model-based reconstruction, inverse problems, hyperspecral.**

I. Introduction

NEUTRONS, unlike X-rays, protons, or electrons, primarily interact with the nucleus rather than the electron shell of atoms, and thus neutron radiography can offer complementary contrast mechanisms to more conventional radiography probes [1]. While X-rays generally get attenuated more by heavier isotopes, this simple relationship does not hold for neutron attenuation. Neutron imaging thus enables the non-destructive evaluation of nuclear fuel, bulk objects, and other materials formed of heavy nuclei [2], while revealing (X-ray-transparent) features such as plant roots and soil water [3], [4]. Applications range from direct methods such as transmission radiography and tomography as well as indirect methods that leverage neutron diffraction and small angle scattering to determine crystal structures, shapes of biological molecules as well as atomic resolution techniques such as neutron holography [2], [5], [6]. In addition, simultaneous X-ray and neutron tomography can provide multimodal attenuation mapping such as the mechanical degradation (via X-rays) as well as chemical diffusion process (via neutrons) in lithium batteries [7], [8].

Neutron time-of-flight (TOF) imaging is a promising imaging technique that exploits the property that neutrons travel with a velocity that depends on their energy. At advanced neutron source facilities, such as ISIS [9], LANSCE [10], SNS [11], and J-PARC [12] spallation neutrons are pulsed and moderated down to yield a broad spectrum of energies. These types of neutron sources allow for neutron TOF measurements, where neutron energies are determined by the time it takes to traverse a known distance between the source and the detector. Thus, pulsed neutron TOF measurements are inherently hyperspectral, and can be used to measure neutron absorption or diffraction as a function of energy [13], [14], [15], [16] facilitating, for example, 2D temperature mapping [17], [18] through Doppler broadening of neutron absorption resonances as well as neutron diffraction imaging techniques for identification of crystal structure and material strains [19], [20].

This paper deals with the problem of reconstructing isotopic densities from neutron TOF transmission measurements given the knowledge of isotope-specific neutron cross section spectra. The neutron energies suitable for this modality range from approximately 1 eV to 10 k eV, categorized as resonance neutrons [16]. Absorption resonances are isotope specific and increase the attenuation of neutrons by orders of magnitude within a narrow energy range [21]. Quantitatively accurate isotope reconstruction is very challenging for a number of reasons. TOF neutron imaging measurements are typically exceptionally noisy, with average neutron counts as low as only 2 counts per measurement bin after several hours of measuring. This is mainly because each measurement bin only corresponds to a single small pixel ($\lesssim 100\,\mu$m) and a short TOF window ($\lesssim 100$ ns) and because even the most advanced neutron sources emit several orders of magnitude fewer particles than typical X-rays sources [22], [23]. In addition, the measurements contain

Manuscript received 10 February 2023; revised 11 September 2023; accepted 3 December 2023. Date of publication 21 December 2023; date of current version 2 February 2024. This work was supported in part by the Laboratory Directed Research and Development program of Los Alamos National Laboratory under Project 20200061DR, and in part by NSF under Grant CCF-1763896. The associate editor coordinating the review of this manuscript and approving it for publication was Dr. Petros T. Boufounos. *(Corresponding author: Thilo Balke.)*

Thilo Balke and Brendt Wohlberg are with Theoretical Division, Los Alamos National Laboratory, Los Alamos, NM 87545 USA (e-mail: thilo.balke@gmail.com; brendt@lanl.gov).

Alexander M. Long and Sven C. Vogel are with the Materials Science and Technology Division, Los Alamos National Laboratory, Los Alamos, NM 87545 USA (e-mail: alexlong@lanl.gov; sven@lanl.gov).

Charles A. Bouman is with the School of ECE and BME of Purdue University, West Lafayette, IN 47907 USA (e-mail: bouman@purdue.edu).

Digital Object Identifier 10.1109/TCI.2023.3345635

substantial background counts which are typically about as strong as the signal itself [24]. Finally, the measurement physics are highly non-linear due to the non-linear absorption, the large dynamic range of the spectral neutron responses of the nuclei, and the effects of the extended pulse duration of the neutron beam, an energy-dependent phenomenon that is caused by the moderation process [16].

The usual method for low-noise measurements [25], [26], [27], [28] is to first compute a transmission spectrum (i.e. open beam normalized transmission measurement) from the TOF data and then to process it with software packages such as SAMMY [29], CONRAD [30] or REFIT [31]. However, these software packages require relatively low-noise estimates of the transmission spectrum as input. In addition, since these software packages are primarily designed for the analysis of individual neutron spectra, they would be very slow when applied to a large array of pixels.

In an imaging application low-noise spectra can be obtained by selecting and averaging regions of interest which can then be processed as a 1D signal [24], [32]. However, the averaging does not yield density estimates on a per-pixel basis, so the problem is shifted to the accurate estimation of transmission spectra at each pixel. It is due to this difficulty that the vast majority of papers on neutron resonance imaging is limited to 2D mapping of isotopes rather than quantification of isotope densities. Our work here aims to overcome these shortcomings.

The transmission spectrum is the expected ratio of the sample and open beam scans, both of which must be corrected for the severe background and beam non-uniformity. There are a number of reasons for the difficulty of accurately estimating these transmission spectra. Although explicit models of the background have been proposed [26], there are no widely accepted methods for jointly estimating background and beam non-uniformity. Moreover, these problems are exacerbated by the need to separately estimate the transmission at each pixel. This means that the spatio-temporal non-uniformity in the background and beam-profile must be accounted for along with the very high level of neutron counting noise. Importantly, since the transmission spectrum estimate is a ratio of two very noisy signals, the resulting spectrum is even noisier.

Notably among the early efforts of estimating 2D and 3D isotope densities are the work of Sato, Kamiyama, et al. [17], [33]. Here a large 8×8 pixel-coarse imaging detector is used to yield low-noise measurements. In addition, the effects of background events were neglected. In [34] a similarly sized detector was used where the estimation was based on the assumption that the isotope densities are simply proportional to the area of the transmission resonance dips. Losko, Vogel et al. [35], [36] accomplished density estimates with a pixel-dense imaging detector. Similar to the previous cases, the transmission spectra are relatively low noise likely due to a combination of much larger TOF bins or spatial denoising pre-processing. Such measures limit spatial and temporal resolution while allowing for only restricted energy range to only about 10 eV. Our work here focuses on low count, high noise measurements.

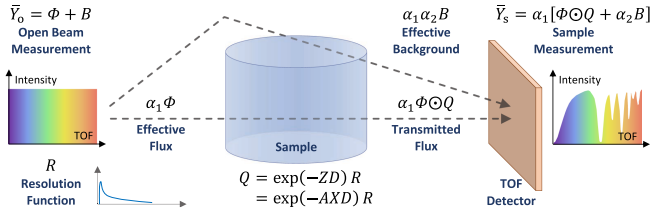

Fig. 1. Illustration of the neutron flight path. A neutron pulse is emitted from the source, attenuated as it passes through the sample, and then detected by a high-speed camera. The time-of-flight (TOF) is used to separate neutrons into a large number of spectral components. The background is illustrated as a jagged line since scattering is assumed to be one source of background.

Previously we proposed a method [37] based on a linearized model and the assumption of opaque "black resonances" [38] to estimate the background counts. While this research demonstrates fast and semi-quantitative results, it has a number of limitations. First, black resonances are not always available or entirely opaque after the blur caused by the extended pulse shape (see Appendix A). Second, the linearized model may not be sufficiently accurate as it neglects to model the extended pulse duration and model the counting noise adequately. Third, this approach implicitly still first estimates the very noisy transmission spectra and as a consequence densities of highly attenuating isotopes can be strongly under-estimated. (See the ^{238}U and ^{240}Pu estimates in Table 2 of [37].)

In this paper, we present the Time-of-flight Resonance Imaging with Neutrons for Isotopic Density Inference (TRINIDI) algorithm. An open-source Python implementation [39] is available in the spirit of reproducible research. Our model-based iterative reconstruction (MBIR [40], [41], [42], [43]) algorithm is based on a two-step process in which we first estimate the neutron flux and background, and then estimate the areal density of each isotope. Importantly, the initial computation of transmission spectra is avoided by modeling the neutron measurement in their native counting domain. Both components are based on the inversion of a forward model that accounts for the highly non-linear absorption, extended pulse duration, and Poisson noise, while also modeling the very substantial space and energy varying background. To do this, we formulate the non-linear inverse problem as two optimization problems that are solved in sequence.

We perform numerical experiments on both simulated and measured data that demonstrate the ability of TRINIDI to reconstruct quantitatively accurate isotopic areal density from 2D data. Finally, we use a series of 2D views of a nuclear fuel sample that were experimentally measured at the LANSCE facility [10] to compute a quantitatively accurate 3D reconstruction of the fuel sample's material composition.

II. The Neutron Imaging System

Fig. 1 illustrates the major components of a neutron beamline. Each pulse contains neutrons with a wide range of energies. The flux neutrons are (quasi-)exponentially attenuated as they pass through a sample, and finally, they are detected by a high speed imaging detector that collects approximately 2000 equi-spaced

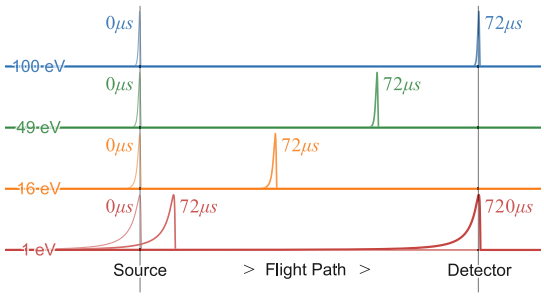

Fig. 2. Propagation of a neutron pulse through an $L = 10$ m flight path. Higher energies correspond to shorter TOFs. The pulse is energy-dependent.

frames at a rate of 30 ns per frame. The background events are also counted by the detector and are assumed to derive from a variety of scattering events in the flight path.

Neutrons, unlike photons, have non-zero mass, so their energy is a function of their velocity, which is in turn a function of their TOF. Consequently, each TOF corresponds to a distinct neutron energy, and the set of images represent a spectral decomposition of the detected neutrons. The neutron velocities are sufficiently low for relativistic effects to be ignored, so the kinetic energy of the neutron is given by

$$E = \frac{1}{2}mv^2 = \frac{1}{2}m\left(\frac{L}{t}\right)^2 \tag{1}$$

where $m \approx 1.045 \times 10^{-8}\,\text{eVs}^2/\text{m}^2$ is the mass,[1] v the velocity, and t the TOF of a neutron and L is the flight path length.[2]

Fig. 2 illustrates the propagation of a neutron pulse through an $L = 10$ m flight path. For this distance, a 1 eV neutron corresponds to a TOF of 720 μs, and a 100 eV neutron corresponds to a TOF of 72 μs. Notice that the higher energy neutrons travel faster, and a $100\times$ increase in energy results in a $10\times$ decrease in TOF.

Notice that the initial pulse is not instantaneous. This means that neutrons with a particular energy may arrive over a range of TOFs. Equivalently, the arrival time does not precisely determine the energy of the neutron. A wider pulse has the effect of blurring absorption features in the time domain and thus limiting the temporal resolution of the imaging system.[3] A longer flight path reduces the blurring,[4] but also reduces the overall flux via the inverse-square law. There is therefore an inherent trade-off between temporal resolution and neutron flux. Lastly, notice that the duration of the pulse is energy-dependent.[5] Accurate

[1] We use $E = mc^2$ to express the unit of mass in terms of eV.

[2] This means that $t \propto \frac{1}{\sqrt{E}}$, and we use TOF and energy interchangeably

[3] similar to a pinhole camera where a wider aperture causes spatial blurring.

[4] The absolute temporal blur is independent of the flight path length. However the longer the flight path the more the time-of-arrival is dominated by the velocity (energy) of the neutron as opposed to the uncertainty in the time the neutron enters the flight path. This effect reduces the relative blur observed at the detector plane.

[5] The energy-dependence of the pulse length comes from the moderation process, a mechanism to create a wide spectrum from a high-energy pulse. Lower energy neutrons are emitted with a longer pulse since there is a larger number of possible collisions in the moderator to arrive at that lower energy.

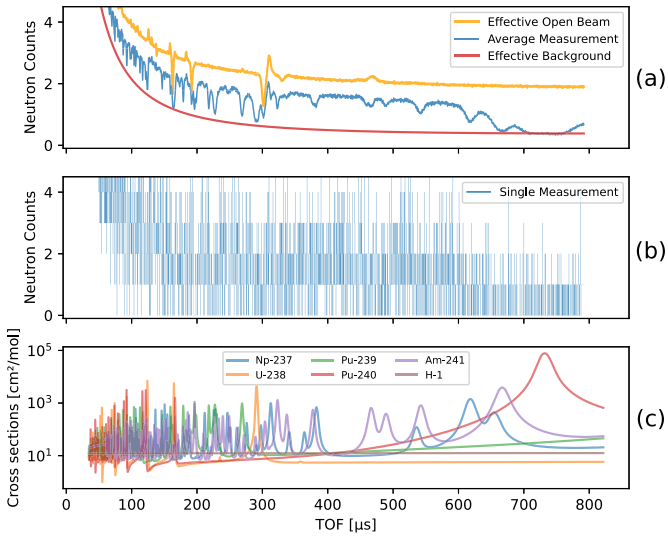

Fig. 3. Spectral characteristics of neutron data as a function of TOF. (a) Typical neutron measurement averaged over many pixels (blue), background neutron counts (red), open beam measurement (yellow). (b) Neutron counts for a single pixel. (c) Neutron cross sections for the isotopes in the sample.

modeling of this effect will prove to be very important in solving our problem.

Our experiments will focus on neutron energies in the range of approximately 1 eV to 100 eV, i.e. resonance region neutrons. At resonances, the interaction probability of an incident neutron can increase by orders of magnitude and cause strong, isotope specific attenuation peaks. Below 1 eV isotopes usually do not have neutron resonances, and thus do not provide sufficient isotope-specific characteristics. At energies above about 100 eV the neutron resonances are so dense that the inherent temporal blur due to the neutron pulse renders individual resonances unresolvable. Furthermore, at such high energies, the neutron counts are dominated by background, which makes the very noisy signal less useful.

Fig. 3(a) shows a neutron spectrum as a function of the TOF. The blue line shows the number of counts averaged over many pixels of the measured spectrum through a sample. Notice that the spectrum shows a great deal of fine structure, i.e. the neutron resonances, that can be used to distinguish different isotopes. Since neutrons interact with the nuclei, these characteristic resonances can be used to distinguish between different isotopes of the same element, such as the fissile ^{235}U and the non-fissile ^{238}U uranium isotopes. The red line shows the background counts which are quite large, and can result from a wide range of scattering effects in the flight path and sample. Finally, the yellow line shows the open beam measurement that results from a combination of the flux and the background events. Importantly, the background is large and the flux has a great deal of variation, so both must be accurately modeled in order to produce an accurate reconstruction of a sample.

Fig. 3(b) shows a plot of a spectral neutron measurement of a single pixel. Since the measurement consists of neutron counts, it is discrete, and it is clear that for individual pixels the signal-to-noise (SNR) ratio is very low. Neutron TOF imaging is challenging due to the very low SNR.

Finally, Fig. 3(c) illustrates the cross section of various isotopes in the sample, in units of $\mathrm{cm}^2/\mathrm{mol}$, as a function of neutron TOF. The concept of a neutron cross section is used to express the likelihood of interaction between an incident neutron and a target nucleus. As the cross section of the material increases, it more strongly attenuates the neutrons and reduces the transmission. For the purposes of this research, these cross section spectra are considered known[6] for particular isotopes that make up the sample.

As an example, imagine a sample made of a single isotope with a known cross section of $\mathbf{d}_j$ $[\mathrm{cm}^2/\mathrm{mol}]$ at TOF bin j. Furthermore, assume that the sample is of uniform thickness ℓ $[\mathrm{cm}]$, with mass density ρ $[\mathrm{g}/\mathrm{cm}^3]$, and molar mass M $[\mathrm{g}/\mathrm{mol}]$, then it has a uniform areal density of

$$z = \frac{\ell \rho}{M} \,. \qquad [\mathrm{mol}/\mathrm{cm}^2] \tag{2}$$

Using Beer's Law, we would expect the transmission of the neutrons through the material at TOF bin, j, to be

$$\mathbf{q}_j = \exp\left\{-z\mathbf{d}_j\right\} \,.$$

Our first goal will be to estimate the areal density, z, for each pixel and each material in the sample. The areal density is predominantly desired with a quasi-2D, flat sample such as a foil or a physical slice of a larger sample.

Our second goal will be to estimate the volumetric density for each isotope in the sample. This is important when the sample is an arbitrarily shaped 3D object, such as the nuclear fuel sample used in our experiments. In this case, our goal is to reconstruct the 3D volumetric density, x, where

$$x = \frac{\rho}{M} \,. \qquad [\mathrm{mol}/\mathrm{cm}^3] \tag{3}$$

We can estimate x for each voxel and material in the sample by extracting the areal densities for each rotational view followed by tomographic reconstruction.

III. Single-Radiograph Forward Model

In this section, we derive our forward model for the hyperspectral neutron measurements of a radiograph. Our goal will be to estimate a matrix $Z \in \mathbb{R}^{N_\mathrm{p} \times N_\mathrm{m}}$ where N_p is the number of scalar projections through a sample (pixels) and N_m is the number of unique isotopes that make up the sample. Then $Z_{i,m}$ represents the areal density in units of $\mathrm{mol}/\mathrm{cm}^2$ of the ith projection through a sample for the mth isotope.

The matrix $D \in \mathbb{R}^{N_\mathrm{m} \times N_\mathrm{F}}$ denotes the cross section dictionary in units of $\mathrm{cm}^2/\mathrm{mol}$ for N_F neutron energies. I.e. $D_{m,j}$ is the cross section for material m at TOF j. Notice that each resonant isotope in the sample must be accounted for because distinct isotopes typically have distinct spectral signatures.

Assuming the conventional Beer-Lambert's law attenuation model, the expected measured neutron counts would be

$$\bar{Y}_\mathrm{s} = \alpha_1 \left[\Phi \odot \exp\left\{-ZD\right\} + \alpha_2 B\right] \,,$$

where α_1 and α_2 are positive scalars, the symbol $\odot$ is the Hadamard product operator, $\Phi_{i,j}$ is the neutron flux, and $B_{i,j}$ is the background for projection i and TOF j, respectively.

The flux, Φ, and background, B, are important scan parameters that vary as a function of position and energy. In X-ray imaging, the background is relatively small and thus the flux can be accurately measured with an "open beam" calibration procedure. However, in neutron imaging, the background tends to be quite large, somewhat sample dependent, and difficult to measure separately. Consequently, it is also very difficult to measure the flux directly from a single open beam measurement. Therefore, a major challenge will be to formulate an imaging methodology that allows us to recover both the flux and background from available measurements.

From Section II, we know that the neutron TOF varies with energy. However, in practice, the measured time of arrival (TOA) does not exactly determine the theoretical time of flight (TOF) of the neutron due to uncertainty in the time the neutron is emitted. The neutrons are emitted in a causal pulse distribution with a long tail that has significant time duration as compared to the sampling rate of the detector camera. A neutron with a specific energy ($\leftrightarrow$ TOF) therefore has finite probability of being detected over a range of times ($\leftrightarrow$ TOA).

In order to model this effect, we introduce the resolution function or resolution operator, $R \in \mathbb{R}^{N_\mathrm{F} \times N_\mathrm{A}}$, representing the conditional probability

$$R_{i,j} = \mathbb{P}\left\{\mathrm{TOA} = \mathbf{t}^\mathrm{A}_j \mid \mathrm{TOF} = \mathbf{t}^\mathrm{F}_i\right\} . \tag{4}$$

The measurement bins are uniformly spaced in time, so we denote the vectors of TOF and TOA bins by $\mathbf{t}^\mathrm{F} \in \mathbb{R}^{N_\mathrm{F}}$ and $\mathbf{t}^\mathrm{A} \in \mathbb{R}^{N_\mathrm{A}}$, respectively, such that

$$\mathbf{t}^\mathrm{A}_j = j\,\Delta_\mathrm{t} + t_0$$
$$\mathbf{t}^\mathrm{F}_i = (i - i_0)\,\Delta_\mathrm{t} + t_0$$

where Δ_t is the TOF bin size, t_0 is the time of the first measured bin, and i_0 is a positive integer offset. Importantly, the set of TOF bins is taken to be sufficiently large that it includes any neutron that could possibly contribute to a measurement. This means that the set of TOA bins will be a contiguous subset of the set of TOF bins, and that $N_\mathrm{F} > N_\mathrm{A}$. Equivalently, R is a sparse matrix that is taller than it is wide. Finally, we assume that the columns of R sum to 1, so that $(\forall j) \sum_i R_{i,j} = 1$. In Appendix A we show that this is because the uncertainty in TOA is modeled as a linear combination of temporal convolutions with the neutron pulse shape.

Using this notation, the final equation for the expected measured neutron flux is given by

$$\bar{Y}_\mathrm{s} = \alpha_1 \left[\Phi \odot \left(\exp\left\{-ZD\right\} R\right) + \alpha_2 B\right] \,. \tag{5}$$

Note that both D and R are assumed to be known for the materials of interest and the particular neutron beamline. The unknowns that must be estimated are therefore Z, Φ, B, α_1, and α_2. It is clear that the dimension of the unknowns far exceeds twice the dimension of the measurements, $\bar{Y}_\mathrm{s}$. Consequently, the direct inversion of (5) is very ill-posed.

[6]Cross section spectra are tabulated in databases such as ENDF/B-VIII.0 [44], which are frequently updated through more accurate measurements.

In order to make the inversion problem well posed, we make three additional assumptions. First, assume that we have made an additional open beam measurement, $\bar{Y}_{\mathrm{o}}$, with the sample removed. Second, assume that the flux and background can be modeled with a low rank approximation. And finally, assume there are two regions in our sample measurement, one in which the sample is not present, and another in which the sample has constant, non-zero areal density.

First, we will assume that a second open beam measurement is made with the sample removed. In this case, $Z = \mathbf{0}$, and we have that

$$\bar{Y}_{\mathrm{o}} = \Phi + B\,, \tag{6}$$

which uses the result (50) from Appendix A.

Second, in order to further improve the conditioning of the inversion problem, we will introduce the constraints that the neutron flux and background, Φ and B, can be modeled with a rank-one approximation given by

$$\Phi = \mathbf{v}\boldsymbol{\varphi}^{\top} \tag{7}$$

$$B = \mathbf{v}\mathbf{b}(\boldsymbol{\theta})^{\top}\,, \tag{8}$$

where $\mathbf{v} \in \mathbb{R}^{N_{\mathrm{p}}}$, $\boldsymbol{\varphi} \in \mathbb{R}^{N_{\mathrm{A}}}$, and

$$\mathbf{b}(\boldsymbol{\theta})^{\top} = \exp\{\boldsymbol{\theta}^{\top}P\}\,, \tag{9}$$

where $\boldsymbol{\theta} \in \mathbb{R}^{N_{\mathrm{b}}}$ is a low dimensional parameter vector, and $P \in \mathbb{R}^{N_{\mathrm{b}} \times N_{\mathrm{A}}}$ is a matrix of basis functions used to model the spectral characteristics of the background counts. The specific form of P is given in detail in Appendix B. In order to make the decomposition unique, we will also require that

$$\mathbb{1}^{\top}\mathbf{v} = N_{\mathrm{p}}\,, \tag{10}$$

where $\mathbb{1}$ denotes a column vector of 1's, i.e. $\mathbf{v}$ is normalized so that its components have an average value of 1.

Third, we will assume that in the sample measurement field of view there are two regions of pixels, denoted by Ω_0, the open beam region, and Ω_{z}, the uniformly dense region. In Ω_0 no part of the sample is covering the beam. In Ω_{z} the sample has uniform cross section. More specifically, we assume

$$(\forall i \in \Omega_{\mathrm{z}})\; Z_{i,*} = \mathbf{z}^{\top} \tag{11}$$

$$(\forall i \in \Omega_0)\; Z_{i,*} = \mathbb{0}^{\top}\,, \tag{12}$$

where $\mathbf{z} \in \mathbb{R}^{N_{\mathrm{m}}}$ is an unknown vector of areal densities and $\mathbb{0}$ is a vector of zeros. These regions must be selected by the user based on knowledge of the sample properties, which is feasible in most applications. This can be achieved by leaving a part of the field of view unobscured to derive the Ω_0 region. One possible method to pick the Ω_{z} region is to select a region in *good faith*, perform a material decomposition and then check whether the resulting density, Z, is actually approximately uniform in Ω_{z}. If the sample does not readily provide a region of approximately equal areal density, a calibration sample could be added to the field of view to derive the Ω_{z} region.

Finally, the actual measurements Y_{s} and Y_{o} are assumed to be conditionally Poisson distributed, which is expressed as

$$Y_{\mathrm{s}} \sim \mathrm{Poisson}(\bar{Y}_{\mathrm{s}}) \mid (Z,\, \mathbf{v},\, \boldsymbol{\varphi},\, \boldsymbol{\theta},\, \alpha_1,\, \alpha_2)$$

$$Y_{\mathrm{o}} \sim \mathrm{Poisson}(\bar{Y}_{\mathrm{o}}) \mid (\mathbf{v},\, \boldsymbol{\varphi},\, \boldsymbol{\theta})\,. \tag{13}$$

IV. Estimation of Nuisance Parameters

In this section, we describe our procedure for estimating the nuisance parameters, $\mathbf{v}$, $\boldsymbol{\varphi}$, $\boldsymbol{\theta}$, α_1, and α_2. This is a challenging problem because it is equivalent to estimation of the background, which tends to be large and spatially variable in neutron imaging.

We start by estimating $\mathbf{v}$ by observing that columns of the open beam scan, $\bar{Y}_{\mathrm{o}}$, must all be proportional to $\mathbf{v}$, and that $\mathbb{1}^{\top}\hat{\mathbf{v}} = N_{\mathrm{p}}$. From this we obtain the estimate

$$\hat{\mathbf{v}} = N_{\mathrm{p}}\frac{Y_{\mathrm{o}}\mathbb{1}}{\mathbb{1}^{\top}Y_{\mathrm{o}}\mathbb{1}}\,. \tag{14}$$

Intuitively, this estimate simply averages the columns of Y_{o} and scales the result so that (10) holds. While this estimator is not optimal for Poisson noise, we have found that it works well given the large number of pixels.

As stated in (11) and (12), the measurement contains a uniformly dense region, Ω_{z}, and a open beam region, Ω_0. Then for each pixel in the region Ω_{z}, the theoretical transmission spectrum through the sample is given by

$$\mathbf{q}(\mathbf{z})^{\top} = \exp\left\{-\mathbf{z}^{\top}D\right\}R\,, \tag{15}$$

where $\mathbf{q}(\mathbf{z}) \in \mathbb{R}^{N_{\mathrm{A}}}$ is the vector of transmission resulting from the material areal densities, $\mathbf{z}$. For each pixel in the region Ω_0 we observe 100% transmission in the open beam region,

$$\mathbf{q}(\mathbb{0})^{\top} = \mathbb{1}^{\top} \tag{16}$$

where we use the fact that $\mathbb{1}^{\top}R = \mathbb{1}^{\top}$, shown in Appendix A.

Let $\boldsymbol{\omega}_0 \in \mathbb{R}^{N_{\mathrm{p}}}$ and $\boldsymbol{\omega}_{\mathrm{z}} \in \mathbb{R}^{N_{\mathrm{p}}}$ be a weighting vectors that take the averages over pixels in those regions, Ω_0 and Ω_{z}, respectively. More precisely, let

$$(\boldsymbol{\omega}_0)_i = \begin{cases} \frac{1}{|\Omega_0|} & \text{if } i \in \Omega_0 \\ 0 & \text{otherwise} \end{cases}$$

$$(\boldsymbol{\omega}_{\mathrm{z}})_i = \begin{cases} \frac{1}{|\Omega_{\mathrm{z}}|} & \text{if } i \in \Omega_{\mathrm{z}} \\ 0 & \text{otherwise} \end{cases}\,.$$

Then define the following three averages:

$$\bar{\mathbf{y}}_{\mathrm{o}}^{\top} = \frac{\mathbb{1}^{\top}\bar{Y}_{\mathrm{o}}}{\mathbb{1}^{\top}\mathbf{v}} \tag{17}$$

$$\bar{\mathbf{y}}_{\mathrm{sz}}^{\top} = \frac{\boldsymbol{\omega}_{\mathrm{z}}^{\top}\bar{Y}_{\mathrm{s}}}{\boldsymbol{\omega}_{\mathrm{z}}^{\top}\mathbf{v}} \tag{18}$$

$$\bar{\mathbf{y}}_{\mathrm{s0}}^{\top} = \frac{\boldsymbol{\omega}_0^{\top}\bar{Y}_{\mathrm{s}}}{\boldsymbol{\omega}_0^{\top}\mathbf{v}}\,. \tag{19}$$

By using (17), (6), (7), and (8), we then have that

$$\begin{aligned}\bar{\mathbf{y}}_{\mathrm{o}}^{\top} &= \frac{\mathbb{1}^{\top}\bar{Y}_{\mathrm{o}}}{\mathbb{1}^{\top}\mathbf{v}} = \frac{\mathbb{1}^{\top}}{\mathbb{1}^{\top}\mathbf{v}}(\Phi + B) \\ &= \frac{\mathbb{1}^{\top}\mathbf{v}}{\mathbb{1}^{\top}\mathbf{v}}(\boldsymbol{\varphi} + \mathbf{b}(\boldsymbol{\theta}))^{\top} = (\boldsymbol{\varphi} + \mathbf{b}(\boldsymbol{\theta}))^{\top}\,.\end{aligned} \tag{20}$$

Rearranging terms then yields the following result

$$\boldsymbol{\varphi} = \bar{\mathbf{y}}_{\mathrm{o}} - \mathbf{b}(\boldsymbol{\theta})\,. \tag{21}$$

Next, by using (18), (5), (7), (8), and (15) along with the expression for $\boldsymbol{\varphi}$ from (21), we can derived the following expression for the average $\bar{\mathbf{y}}_{\mathrm{sz}}^{\top}$ given by

$$\begin{aligned}\bar{\mathbf{y}}_{\mathrm{sz}}^{\top} &= \frac{\boldsymbol{\omega}_{\mathrm{z}}^{\top}\bar{Y}_{\mathrm{s}}}{\boldsymbol{\omega}_{\mathrm{z}}^{\top}\mathbf{v}} \\ &= \frac{\alpha_1}{\boldsymbol{\omega}_{\mathrm{z}}^{\top}\mathbf{v}}\boldsymbol{\omega}_{\mathrm{z}}^{\top}\left[\Phi \odot \left(\exp\left\{-\mathbb{1}\mathbf{z}^{\top}D\right\}R\right) + \alpha_2 B\right] \\ &= \frac{\alpha_1}{\boldsymbol{\omega}_{\mathrm{z}}^{\top}\mathbf{v}}\boldsymbol{\omega}_{\mathrm{z}}^{\top}\left[(\mathbf{v}\boldsymbol{\varphi}^{\top}) \odot \left(\mathbb{1}\mathbf{q}(\mathbf{z})^{\top}\right) + \alpha_2 \mathbf{v}\mathbf{b}(\boldsymbol{\theta})^{\top}\right] \\ &= \alpha_1\left[\boldsymbol{\varphi} \odot \mathbf{q}(\mathbf{z}) + \alpha_2 \mathbf{b}(\boldsymbol{\theta})\right]^{\top} \\ &= \alpha_1\left[(\bar{\mathbf{y}}_{\mathrm{o}} - \mathbf{b}(\boldsymbol{\theta})) \odot \mathbf{q}(\mathbf{z}) + \alpha_2 \mathbf{b}(\boldsymbol{\theta})\right]^{\top}. \end{aligned} \tag{22}$$

Similar to (22), an expression for $\bar{\mathbf{y}}_{\mathrm{s0}}^{\top}$ can be found using (19) and (16),

$$\begin{aligned}\bar{\mathbf{y}}_{\mathrm{s0}}^{\top} = \frac{\boldsymbol{\omega}_0^{\top}\bar{Y}_{\mathrm{s}}}{\boldsymbol{\omega}_0^{\top}\mathbf{v}} &= \alpha_1\left[(\bar{\mathbf{y}}_{\mathrm{o}} - \mathbf{b}(\boldsymbol{\theta})) \odot \mathbf{q}(\mathbf{z}) + \alpha_2 \mathbf{b}(\boldsymbol{\theta})\right]^{\top} \\ &= \alpha_1\left[\bar{\mathbf{y}}_{\mathrm{o}} + (\alpha_2 - 1)\mathbf{b}(\boldsymbol{\theta})\right]^{\top}. \end{aligned} \tag{23}$$

By substituting in the measured neutron counts (Y_{s}, Y_{o}) for the expected measurements ($\bar{Y}_{\mathrm{o}}$, $\bar{Y}_{\mathrm{s}}$) in (22) and (23), we can formulate a loss function. Then we can estimate the nuisance parameters by minimizing this loss function:

$$\begin{aligned}(\hat{\mathbf{z}}, \hat{\alpha}_1, \hat{\alpha}_2, \hat{\boldsymbol{\theta}}) = \underset{\mathbf{z},\alpha_1,\alpha_2,\boldsymbol{\theta}}{\arg\min} \Big\{ &\left\|\mathbf{y}_{\mathrm{sz}} - \mathbf{f}(\mathbf{z}, \alpha_1, \alpha_2, \boldsymbol{\theta})\right\|^2 \\ &+\beta\left\|\mathbf{y}_{\mathrm{s0}} - \mathbf{f}(\mathbb{0}, \alpha_1, \alpha_2, \boldsymbol{\theta})\right\|^2 \Big\} \\ \text{s.t.} \quad \mathbf{z} &\geq \mathbb{0} \\ \alpha_1, \alpha_2 &\geq 0 \\ \boldsymbol{\theta} &\in \mathbb{R}^{N_{\mathrm{b}}}, \end{aligned} \tag{24}$$

where the forward operators are defined by,

$$\mathbf{f}(\mathbf{z}, \alpha_1, \alpha_2, \boldsymbol{\theta}) = \alpha_1\left[(\mathbf{y}_{\mathrm{o}} - \mathbf{b}(\boldsymbol{\theta})) \odot \mathbf{q}(\mathbf{z}) + \alpha_2 \mathbf{b}(\boldsymbol{\theta})\right] \tag{25}$$

$$\mathbf{f}(\mathbb{0}, \alpha_1, \alpha_2, \boldsymbol{\theta}) = \alpha_1\left[\mathbf{y}_{\mathrm{o}} + (\alpha_2 - 1)\mathbf{b}(\boldsymbol{\theta})\right], \tag{26}$$

and the scalar β is a weighting parameter that balances the associated costs between solving (22) and (23). Since $\boldsymbol{\omega}_0^{\top}$ and $\boldsymbol{\omega}_{\mathrm{z}}^{\top}$ perform averaging over many pixels, the Poisson distribution approximates a Gaussian via the Central Limit Theorem, which we use as a justification for the use of Least Squares estimators in (24).

This optimization yields the estimates $\hat{\mathbf{z}}$, $\hat{\alpha}_1$, $\hat{\alpha}_2$, and $\hat{\boldsymbol{\theta}}$. The final parameter, $\boldsymbol{\varphi}$, is then estimated via (21) as

$$\hat{\boldsymbol{\varphi}} = \mathbf{y}_{\mathrm{o}} - \mathbf{b}(\hat{\boldsymbol{\theta}}), \tag{27}$$

and the estimates for the flux and background

$$\begin{aligned}\hat{\Phi} &= \hat{\mathbf{v}}\hat{\boldsymbol{\varphi}}^{\top} \\ \hat{B} &= \hat{\mathbf{v}}\mathbf{b}(\hat{\boldsymbol{\theta}})^{\top}. \end{aligned} \tag{28}$$

V. Areal Density Reconstruction

In this section, we describe how we reconstruct the isotope areal density, Z, based on a statistical model of the neutron counting statistics. The estimated nuisance parameters from Section IV are considered known at this point.

We assume that the actual neutron sample measurements, Y_{s}, are independent Poisson distributed with conditional mean $\bar{Y}_{\mathrm{s}}$. More precisely, if we define the operator

$$F(Z) = \hat{\alpha}_1\left[\hat{\Phi} \odot \left(\exp\left\{-ZD\right\}R\right) + \hat{\alpha}_2\hat{B}\right], \tag{29}$$

then we assume that

$$Y_{\mathrm{s}} \sim \mathrm{Poisson}(F(Z)) \mid Z,$$

and the conditional mean of the observations given the unknown Z is therefore

$$\mathbb{E}\left[Y_{\mathrm{s}}|Z\right] = F(Z).$$

For a Poisson random matrix Y with mean Λ, the negative log-likelihood is

$$\begin{aligned}\mathcal{L}(Y|\Lambda) &= -\log f_{Y|\Lambda}(Y|\Lambda) \\ &= \sum_{i,j} \Lambda_{i,j} - Y_{i,j}\log\Lambda_{i,j} + \log(Y_{i,j}!). \end{aligned}$$

Then our maximum likelihood estimate for the material areal density is given by

$$\hat{Z} = \underset{Z\in\mathbb{R}^{N_{\mathrm{p}}\times N_{\mathrm{m}}}}{\arg\min}\ \mathcal{L}(Y_{\mathrm{s}}|F(Z)). \tag{30}$$

VI. Volumetric Density Reconstruction

In this section we describe a 3D tomographic extension to the 2D case that is possible when measurements of multiple rotational views are available. This will be a two step approach involving first reconstructing the areal densities, Z, for each view, and then performing tomographic reconstruction of the volumetric densities, X.

Let $\{Y_{\mathrm{s}}^{(k)}\}_{k=1}^{N_{\mathrm{r}}}$ be the set of N_{r} measurements at distinct views. Corresponding to these measurements, we will reconstruct N_{r} areal density views $\{Z^{(k)}\}_{k=1}^{N_{\mathrm{r}}}$ using the material decomposition of (30). We assume all nuisance parameters except α_1 are independent of view index and thus only need to be computed once from a single view. The $\{\alpha_1^{(k)}\}_{k=1}^{N_{\mathrm{r}}}$ set of parameters are assumed to be dependent on the view index, k, and are estimated using the closed form expression[7]

$$\hat{\alpha}_1^{(k)} = \frac{\left[\mathbf{y}_{\mathrm{s0}}^{(k)}\right]^{\top}\mathbb{1}}{\left[\mathbf{y}_{\mathrm{o}} + (\hat{\alpha}_2 - 1)\mathbf{b}(\hat{\boldsymbol{\theta}})\right]^{\top}\mathbb{1}}, \tag{31}$$

where $\left[\mathbf{y}_{\mathrm{s0}}^{(k)}\right]^{\top} = \frac{\left([\boldsymbol{\omega}_0^{(k)}]^{\top}Y_{\mathrm{s}}^{(k)}\right)}{\left([\boldsymbol{\omega}_0^{(k)}]^{\top}\mathbf{v}\right)}$ correspond to the user selected open beam regions, $\Omega_0^{(k)}$, while $\Omega_{\mathrm{z}}^{(k)}$ regions need not necessarily be available for every rotational view.

[7]This expression is a corollary of (23) and its derivation is omitted.

The estimated set of areal densities is stacked, and we assume the following decomposition

$$\hat{Z} = \begin{bmatrix} \hat{Z}^{(1)} \\ \vdots \\ \hat{Z}^{(N_\mathrm{r})} \end{bmatrix} = AX, \tag{32}$$

where the areal density estimates, $\hat{Z} \in \mathbb{R}^{(N_\mathrm{r}N_\mathrm{p})\times N_\mathrm{r}}$, are in units of mol/cm^2, the tomographic projector, $A \in \mathbb{R}^{(N_\mathrm{r}N_\mathrm{p})\times N_\mathrm{v}}$, is in units of cm, and the volumetric densities, $X \in \mathbb{R}^{N_\mathrm{v}\times N_\mathrm{m}}$ are in units of mol/cm^3 and comprised of N_v voxels. Then $X_{j,m}$ represents the volumetric density of the jth voxel for the mth isotope in the sample, and $A_{i,j}$ integrates along the tomographic projection line of the jth voxel and the ith measurement projection.

Finally, computing the volumetric densities, X, boils down to solving (32) which can be decomposed by columns:

$$\begin{bmatrix} | & & | \\ \hat{Z}_{*,1} & \dots & \hat{Z}_{*,N_\mathrm{m}} \\ | & & | \end{bmatrix} = A \begin{bmatrix} | & & | \\ X_{*,1} & \dots & X_{*,N_\mathrm{m}} \\ | & & | \end{bmatrix}.$$

Consequently for each isotope the volumetric density $X_{*,m}$ is reconstructed from $\hat{Z}_{*,m}$ as the solution of

$$\hat{X}_{*,m} = \underset{0\le\mathbf{x}\in\mathbb{R}^{N_\mathrm{p}}}{\arg\min} \left\{ \|A\mathbf{x} - \hat{Z}_{*,m}\|^2 + r_m(\mathbf{x}) \right\}, \tag{33}$$

using a tomographic reconstruction algorithm, where $r_m(\cdot)$ is a 3D regularization term of the mth isotope. Although (33) specifies the use of MBIR reconstruction, other tomographic reconstruction methods can be used. However, we note that neutron tomography typically must use sparse views due to the slow view acquisition times, and that traditional CT reconstruction methods, such as filtered back projection, result in severe artifacts for the sparse view case. So we believe that MBIR reconstruction is a good choice for this application.

VII. Optimization Methods

The key steps in the reconstruction of (24) and (30) require the solution of non-convex optimization problems. In this section, we discuss the techniques we use to implement robust strategies for computing their solutions.

A. Preconditioning

A practical issue in optimization is that both (24) and (30) incorporate loss functions with exponential terms such as $\mathbf{b}(\boldsymbol{\theta})^\top = \exp\{\boldsymbol{\theta}^\top P\}$ and $\mathbf{q}(\mathbf{z})^\top = \exp\{-\mathbf{z}^\top D\}R$. These terms can have large dynamic range and can therefore be sensitive to small changes in their arguments.

In order to limit the dynamic range of these exponential terms, we defined P in (51) so that its rows have unit norm. We can do the same for the dictionary matrix D by defining

$$\tilde{D} = C^{-1}D \tag{34}$$

where C is a diagonal matrix such that $C_{i,i} = \|D_{i,*}\|$. However, this also requires that we define the new functions

$$\tilde{\mathbf{q}}(\tilde{\mathbf{z}})^\top = \exp\left\{-\tilde{\mathbf{z}}^\top \tilde{D}\right\} R \tag{35}$$

$$\tilde{F}(\tilde{Z}) = \hat{\alpha}_1 \left[\hat{\Phi} \odot \left(\exp\left\{-\tilde{Z}\tilde{D}\right\} R\right) + \hat{\alpha}_2 \hat{B}\right], \tag{36}$$

that are used to replace the functions of (15) and (29).

After the modified optimization problems are solved, the solution of the original problem can be found using

$$\mathbf{z}^\top = \tilde{\mathbf{z}}^\top C \tag{37}$$

$$Z = \tilde{Z}C\,. \tag{38}$$

B. Initialization

Since the optimization problems are not convex, it is important to select good initializations that lead to solutions that are close to the global minimum. We first focus on the initialization of the optimization in (24) of the nuisance parameter estimation. The initial values that we use are

$$\alpha_2 = 1 \tag{39}$$

$$\alpha_1 = \frac{\boldsymbol{\omega}_0^\top Y_\mathrm{s}}{\boldsymbol{\omega}_0^\top Y_\mathrm{o}} \tag{40}$$

$$\boldsymbol{\theta}^\top = \log\left(\min_i \left\{\frac{(\mathbf{y}_\mathrm{sz})_i}{(\mathbf{y}_\mathrm{o})_i}\right\} \frac{\mathbf{y}_\mathrm{o}}{\alpha_1\alpha_2}\right)^\top P^\dagger \tag{41}$$

$$\mathbf{z}^\top = -\log(\mathbf{q}^\top)(DR)^\dagger\,, \tag{42}$$

where $(\cdot)^\dagger$ denotes the Moore–Penrose pseudoinverse and

$$\mathbf{q} = \left|\frac{\mathbf{y}_\mathrm{s}/\alpha_1 - \alpha_2\mathbf{b}(\boldsymbol{\theta})}{\mathbf{y}_\mathrm{o} - \mathbf{b}(\boldsymbol{\theta})}\right|$$

is the average measured transmission, given the initial nuisance parameters, α_1, α_2, and $\boldsymbol{\theta}$. This initialization is motivated by (23) and the following crude approximations:

$$\hat{\alpha}_2 \approx 1$$

$$\mathbf{y}_{\mathrm{s}0} \approx \hat{\alpha}_1 \left[\mathbf{y}_\mathrm{o} + (\hat{\alpha}_2 - 1)\mathbf{b}(\hat{\boldsymbol{\theta}})\right]$$

$$\hat{\alpha}_1\hat{\alpha}_2\mathbf{b}(\hat{\boldsymbol{\theta}}) \approx \min_i \left\{\frac{(\mathbf{y}_\mathrm{sz})_i}{(\mathbf{y}_\mathrm{o})_i}\right\} \mathbf{y}_\mathrm{o}$$

$$\exp\{-ZD\}R \approx \exp\{-ZDR\}\,.$$

For the optimization of (30), we initialize

$$Z = -\log(Q)(DR)^\dagger\,, \tag{43}$$

where the measured transmission

$$Q = \left|\frac{Y_\mathrm{s}/\hat{\alpha}_1 - \hat{\alpha}_2\hat{B}}{Y_\mathrm{o} - \hat{B}}\right|$$

is computed given the final nuisance parameters.

VIII. Experimental Results

In this section we present results of the TRINIDI algorithm applied to both simulated and experimentally measured data.

Section VIII-A outlines the experimental settings and notes about the evaluation of the results. In Section VIII-B, we demonstrate the method using 2D simulated radiographs. In Section VIII-C, we provide similar 2D results for experimentally measured data using a known phantom. Finally in Section VII-I-D, we present results for fully tomographic 3D reconstruction of nuclear fuel pellets that are verified using independent mass spectroscopy measurements.

A. Methods

Experiments in this work were performed at the Flight-Path-5 beamline at LANSCE [10]. In this facility, high energy spallation neutrons are slowed down by a high intensity ambient temperature water moderator resulting in a 20 Hz pulsed neutron beam with a wide energy spectrum. A detailed description of this facility including a characterization of the incident neutron spectrum can be found in [22].

The neutrons travel along a flight path of length of $L = 10.4$ m through the sample onto a TOF imaging detector. The neutron sensitive multi-channel plate detector works in conjunction with four Timepix readout chips, described in more detail in [45]. The detector has $N_{\mathrm{p}} = 512 \times 512$ pixels with a $55 \times 55\,(\mu\mathrm{m})^2$ pixel pitch i.e. covering a field of view of approximately $28 \times 28\,(\mathrm{mm})^2$, and frames are recorded at a rate of, $\frac{1}{\Delta_{\mathrm{t}}} \approx \frac{1}{30\ \mathrm{ns}} \approx 33.3$ MHz.

The resolution function is modeled as an energy dependent weighted sum of two chi-squared probability density functions based on the work in [46]. As described in Appendix A, the energy dependent pulse shape is approximated by a weighted sum of convolutions of K kernels. We choose $K = 5$ since we found that this gave sufficiently accurate representation of the resolution function.

In order to assess the accuracy of the nuisance parameter estimation of (24), we plot $\mathbf{y}_{\mathrm{s0}}$ (the measurement in the open beam region) and the fit of $\mathbf{y}_{\mathrm{s0}}$ (the effective open beam) given by

$$\mathbf{f}(\mathbb{0}, \alpha_1, \alpha_2, \boldsymbol{\theta}) = \alpha_1 \left[\mathbf{y}_{\mathrm{o}} + (\alpha_2 - 1)\mathbf{b}(\boldsymbol{\theta})\right] \ , \qquad (44)$$

where (44) is the expected measurement when there is 100% transmission (i.e. zero material). We also plot $\mathbf{y}_{\mathrm{sz}}$ (the measurement in the uniformly dense region) and the fit of $\mathbf{y}_{\mathrm{sz}}$ given by

$$\mathbf{f}(\mathbf{z}, \alpha_1, \alpha_2, \boldsymbol{\theta}) = \alpha_1 \left[(\mathbf{y}_{\mathrm{o}} - \mathbf{b}(\boldsymbol{\theta})) \odot \mathbf{q}(\mathbf{z}) + \alpha_2 \mathbf{b}(\boldsymbol{\theta})\right] \ , \qquad (45)$$

where (45) is the expected measurement when there is a uniform material density, $\mathbf{z}$, attenuating the beam. Lastly, we plot the effective background given by

$$\mathbf{f}(\boldsymbol{\infty}, \alpha_1, \alpha_2, \boldsymbol{\theta}) = \alpha_1 \alpha_2 \mathbf{b}(\boldsymbol{\theta}) \, , \qquad (46)$$

where (46) is the expected measurement when there is there is 0 % transmission (i.e. infinite material).

We display normalized density images for more accessible interpretation of our density estimates. The scales of the densities differ widely from one another so that instead of directly displaying the all $Z_{*,m}$ with a different color map, we choose to display all $Z_{*,m}/\mathbf{z}_m$ with the same color map. The scalars $\mathbf{z}_m$ are the ground truth average density of the mth isotope (or some other adequate normalization). Thus, the normalized densities, $Z\,\mathrm{diag}(\mathbf{z})^{-1}$, are unitless, where 1 corresponds to the values of $\mathbf{z}$ i.e. ground truth. A similar treatment is applied to the volumetric densities, X.

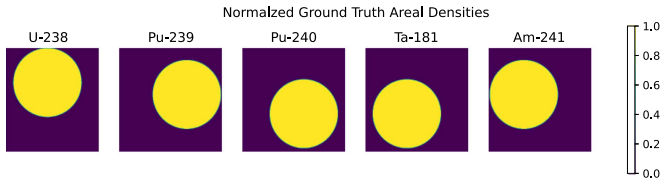

Fig. 4. Normalized ground truth areal densities ($Z\,\mathrm{diag}(\mathbf{z})^{-1}$, [unitless]) used in the simulated data set of Section VIII-B.

Finally, for the cross section dictionary, D, we use tabulated data, of the neutron total cross section at a temperature of 293.6 K from ENDF/B-VIII.0 [44].

We compare our reconstruction results to the reconstruction using the linear model from [37] which we refer to as linear baseline reconstruction or Z^{lin}. In an attempt to further compare our results to existing methods, we tried processing the transmission spectra from our experiments using SAMMY [29]. However, due to the significant noise, we were unable to get the software to function properly.

All tomographic reconstructions were performed using the super-voxel model-based iterative reconstruction (SVMBIR) software package [47], with parameters selected to maximize subjective image quality, and all optimizations were performed using the accelerated proximal gradient method (APGM) with robust line search[8] as part of the scientific computational imaging code (SCICO) software package [48]. The β parameter from (24) is chosen to be equal to 1 in Section VIII-B and Section VIII-D and chosen to be equal to 0 in Section VIII-C because in this experiment, there is no Ω_0 region available. The number of background basis functions is chosen to be $N_{\mathrm{b}} = 5$.

B. 2D Reconstruction From Simulated Data

In this experiment, we reconstruct a 2D phantom from Monte-Carlo simulated data. Fig. 4 illustrates the structure of the simulated 2D phantom which is composed of a series of overlapping disks each formed by a distinct material isotope. The other parameters of the simulation were chosen to approximately mimic a typical experimental scenario.

The ground truth areal densities were chosen to represent $N_{\mathrm{m}} = 5$ distinct isotopes, where each areal density map, $Z_{*,m}$, consists of a disk of constant density $\mathbf{z}_m$ with a surrounding area of zero material. Each map has $N_{\mathrm{p}} = 128 \times 128$ pixels. The numerical values of the densities, $\mathbf{z}$, can be found in Table I and were chosen to yield a visible distribution of resonances in the

[8]This algorithm was selected due to the convenient availability of a reliable implementation rather than any expectation of optimum suitability for this problem, and it is expected that other optimization algorithms may provide faster convergence. In particular, after completion of the computational experiments reported here, we observed that the Broyden–Fletcher–Goldfarb–Shannon (BFGS) algorithm appears to converge significantly faster than APGM.

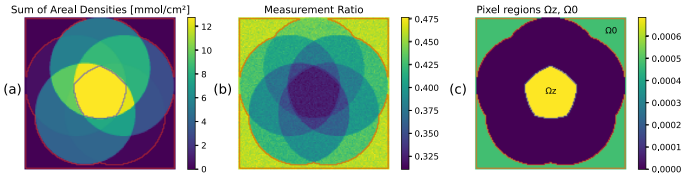

Fig. 5. Open beam region, Ω_0 (red line), and uniformly dense region, Ω_z (blue line), in simulated data set. (a) Sum of ground truth areal densities ($Z\mathbb{1}$). (b) TOF integrated measurement ratio, $\frac{Y_s\mathbb{1}}{Y_o\mathbb{1}}$. (c) Pixel regions: Ω_0 green, Ω_z yellow.

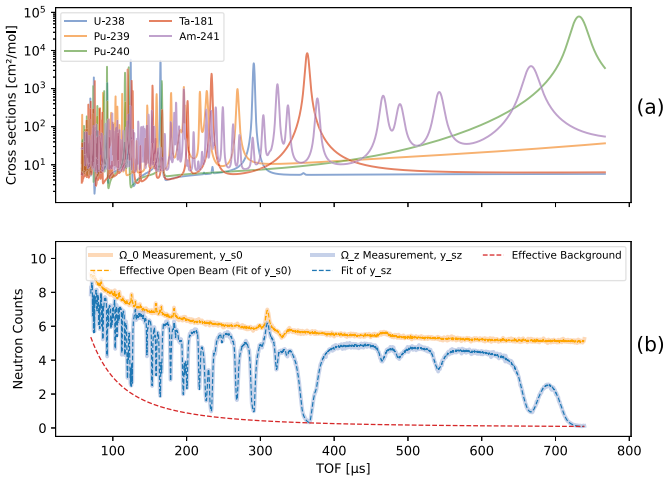

Fig. 6. Nuisance parameter estimation fits of the simulated data set. (a) Cross section dictionary, D, with ^{238}U, ^{239}Pu, ^{240}Pu, ^{181}Ta, and ^{241}Am isotopes in units of $\mathrm{cm}^2/\mathrm{mol}$. (b) Ω_0 measurement $\mathbf{y}_{s0}$ (yellow), effective open beam (yellow dashed), Ω_z measurement $\mathbf{y}_{sz}$ (blue), fit of $\mathbf{y}_{sz}$ (blue dashed), effective background (red dashed).

TABLE I
GROUND TRUTH AND ESTIMATED VALUES OF NUISANCE PARAMETERS FOR THE SIMULATED DATA SAMPLE

Quantity	Ground Truth
$\begin{bmatrix}\text{isotopes}\\ \mathbf{z}^\top\,[\mathrm{mmol/cm^2}]\end{bmatrix}$	$\begin{bmatrix}^{238}\mathrm{U} & ^{239}\mathrm{Pu} & ^{240}\mathrm{Pu} & ^{181}\mathrm{Ta} & ^{241}\mathrm{Am}\\ 5.00 & 3.00 & 0.200 & 4.00 & 0.500\end{bmatrix}$
$\alpha_1,\ \alpha_2$	$0.483,\ \ 0.685$
$\boldsymbol{\theta}^\top$	$\begin{bmatrix}29.9 & -56.1 & 5.39\end{bmatrix}$
Quantity	**Estimates**
$\begin{bmatrix}\text{isotopes}\\ \hat{\mathbf{z}}^\top\,[\mathrm{mmol/cm^2}]\end{bmatrix}$	$\begin{bmatrix}^{238}\mathrm{U} & ^{239}\mathrm{Pu} & ^{240}\mathrm{Pu} & ^{181}\mathrm{Ta} & ^{241}\mathrm{Am}\\ 5.00 & 2.99 & 0.194 & 3.93 & 0.493\end{bmatrix}$
$\hat{\alpha}_1,\ \hat{\alpha}_2$	$0.481,\ \ 0.687$
$\hat{\boldsymbol{\theta}}^\top$	$\begin{bmatrix}27.7 & -59.6 & 3.50\end{bmatrix}$

measurement spectra. The isotopes used are ^{238}U, ^{239}Pu, ^{240}Pu, ^{181}Ta, ^{241}Am and their respective cross sections are shown in Fig. 6(a).

The simulated measurement counts, Y_s and Y_o, were generated by first computing their sample means using (5) and (6), and then generating pseudo-random Poisson samples corresponding to those means. In order to make the simulation representative of a typical physical experiment, the values for $\mathbf{v}$, $\boldsymbol{\theta}$, α_1, α_2, $\boldsymbol{\varphi}$, and the TOF sampling interval are chosen to be the same as the estimates from the real data covered in Section VIII-C.

Fig. 5 shows the summed areal densities over all isotopes, the TOF integrated measurement ratio $\frac{Y_s\mathbb{1}}{Y_o\mathbb{1}}$, and the regions Ω_z

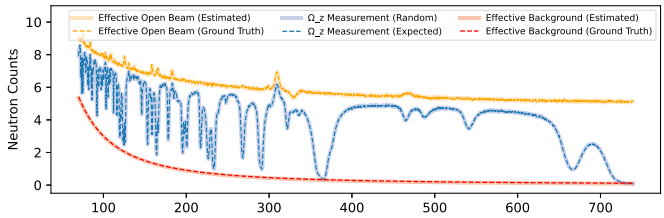

Fig. 7. Comparison of estimated vs. ground truth spectra resulting from the nuisance parameter estimation of the simulated data set.

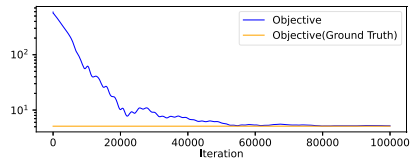

Fig. 8. Convergence of nuisance parameter estimation for simulated data.

and Ω_0 used for this experiment. The set Ω_z was taken to be the region in the center of the phantom in which all the disks overlap, and the set Ω_0 was taken to be the region surrounding the disks that is not covered by any material.

Table I lists the results of the nuisance parameter estimation using (24). Notice that the parameters of interest, $\hat{\mathbf{z}}$, are accurately estimated within approximately 3%. The estimation of the nuisance parameters, α_1, α_2 and $\boldsymbol{\theta}$, is more variable; however, we note that accurate estimation of nuisance parameters may not always be necessary as long as the effective open beam and background are accurately modeled.

Fig. 6(b) shows plots corresponding to the fitted curves of the nuisance parameter estimation. The orange and blue curves are the average sample measurements, $\mathbf{y}_{s0}$ and $\mathbf{y}_{sz}$, and the dashed lines of the same respective colors are their corresponding fits. Note that the measurements and fits visually align very well. The red dashed line is the resulting effective background.

Fig. 7 shows a direct comparison to the ground truth spectra. The effective open beam (yellow lines) and background (red lines) are compared directly their respective ground truth spectra (dashed lines). Notice that all three fits are quite accurate, even though the underlying nuisance parameter estimates in Table I where not as accurate.

Fig. 8 shows the objective of the optimization as a function of iteration number. Although the optimization takes many iterations and is not monotone, the objective eventually converges to approximately the same value as the ground truth.

Fig. 9(a) shows the normalized ground truth areal densities, Fig. 9(b) shows the linear baseline [37] reconstructed areal density, and Fig. 9(c) shows the corresponding TRINIDI reconstructed areal density. The linear baseline reconstruction deviates significantly from the ground truth. Notice that using TRINIDI each isotope map is accurately reconstructed from the simulated data. Also, even though the disks significantly overlap with one another, especially in the center of the field of view, there are no visible artifacts, which is not the case for the linear baseline.

It is worth pointing out that the cross section dictionary, D, contains all five isotopes, however, most pixels in the ground

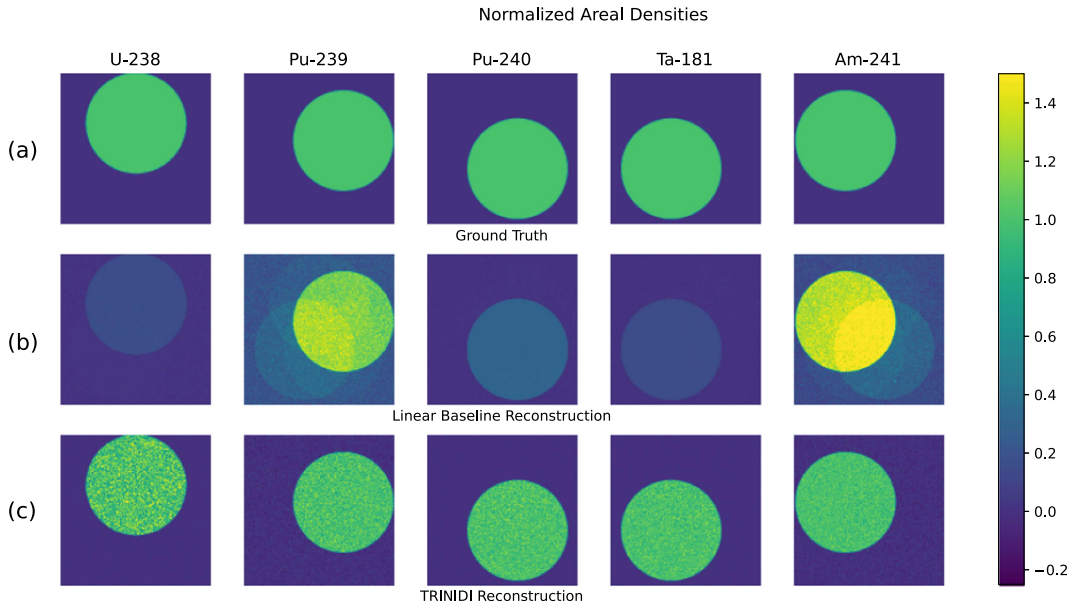

Fig. 9. Normalized areal densities results for the simulated data [unitless]. (a) Normalized ground truth areal density ($Z\,\mathrm{diag}(\mathbf{z})^{-1}$). (b) Normalized linear baseline [37] reconstructed areal density ($Z^{\mathrm{lin}}\,\mathrm{diag}(\mathbf{z})^{-1}$). (c) Normalized TRINIDI reconstructed areal density ($\hat{Z}\,\mathrm{diag}(\mathbf{z})^{-1}$).

TABLE II
MEAN AND STANDARD DEVIATION OF AREAL DENSITY MAPS OF GROUND TRUTH (Z), LINEAR BASELINE RECONSTRUCTION [37] (Z^{lin}), AND TRINIDI RECONSTRUCTION ($\hat{Z}$) IN UNITS OF [MMOL/CM^2] OF THE SIMULATED DATA SAMPLE

Isotopes	Ground Truth	Linear Baseline [37]	TRINIDI
^{238}U	5.0 ± 0.0	0.825 ± 0.082	$\mathbf{5.065 \pm 1.045}$
^{239}Pu	3.0 ± 0.0	3.613 ± 0.336	$\mathbf{3.009 \pm 0.341}$
^{240}Pu	0.2 ± 0.0	0.062 ± 0.001	$\mathbf{0.202 \pm 0.021}$
^{181}Ta	4.0 ± 0.0	0.631 ± 0.021	$\mathbf{4.015 \pm 0.376}$
^{241}Am	0.5 ± 0.0	0.703 ± 0.067	$\mathbf{0.499 \pm 0.039}$

truth do not have all five isotopes present. For example, in the very top-center region only ^{238}U is present. The TRINIDI reconstructions show that ^{238}U is reconstructed accurately as non-zeros while the other isotopes are reconstructed accurately as (close to) zeros. This indicates that overpopulation of the cross section dictionary will likely not result in degradation of the reconstruction, however, we suggest that unnecessary overpopulation should be avoided.

Table II shows the mean and standard deviation of the density estimates, $\hat{Z}_{*,m}$ for each of the disks of material individually compared to the ground truth (Z) and the linear baseline (Z^{lin}). Note that even though there is significant noise, the mean estimates using TRINIDI are very close to the ground truth densities. Also note that the different isotopes have different estimation accuracy. In comparison, the linear baseline estimates are not quantitatively accurate.

Fig. 10 shows the convergence behaviour of the optimization of (30). The final objective is slightly better than the ground truth objective after only about 50 iterations and then converges to its final value. This indicates likely convergence to near the global minimum, however, with possible slight overfitting. Note that the convergence takes significantly fewer iterations as compared to the nuisance parameter estimation.

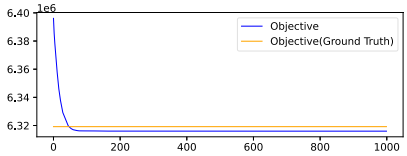

Fig. 10. Convergence of areal density estimation for the simulated data.

C. 2D Reconstruction From Experimental Data

This experiment is similar to the 2D Monte-Carlo simulated experiment of Section VIII-B, but it uses measured data. We use a known, well-defined sample in order to demonstrate the quantitative accuracy of our method with experimentally measured data.

The sample is a stack of uniform tantalum (Ta) and tungsten (W) plates. The plates have thicknesses of $\ell_{\mathrm{Ta}} = 2.42$ mm and $\ell_{\mathrm{W}} = 1.75$ mm. We refer to this sample as the TaW sample. The $N_{\mathrm{A}} = 2260$ TOF bins span an interval from 70.11 μs up to 739.1 μs which corresponds to an energy range of 115.0 eV down to 1.04 eV, respectively. We use a cropped region of the detector of $N_{\mathrm{p}} = 128 \times 128$ pixels.

Fig. 11 shows the TOF integrated measurement ratio, $\frac{Y_{\mathrm{s}}\mathbb{1}}{Y_{\mathrm{o}}\mathbb{1}}$ of the sample. The sample covers the entire field of view and thus there is no set of pixels that is suitable for the open beam region Ω_0. For this reason we choose the parameter $\beta = 0$ in (24), effectively dropping the constraint of jointly solving (23) in the nuisance parameter estimation. Since the sample is assumed to be constant across the field of view, the set Ω_{z} is chosen to be the entire field of view.

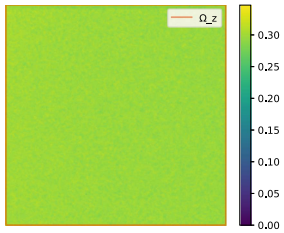

Fig. 11. TOF integrated measurement ratio, $\frac{Y_s \mathbb{1}}{Y_o \mathbb{1}}$, of the TaW sample. Uniformly dense region, Ω_z (red line), open beam region, Ω_0 does not exist for this measurement because the whole field of view is covered by the sample.

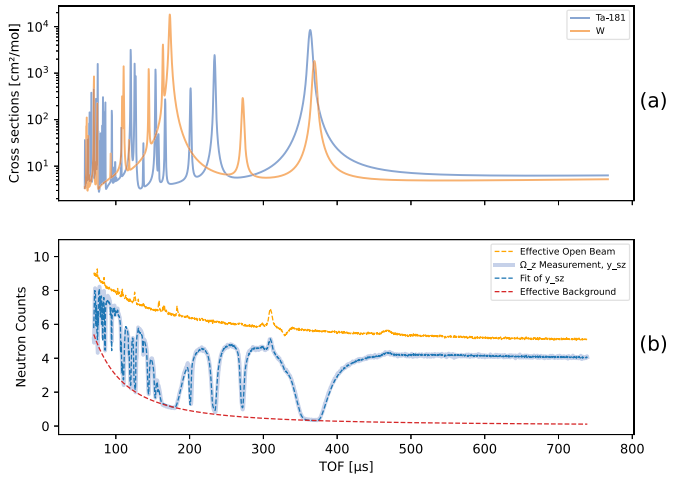

Fig. 12. Nuisance parameter estimation fits of the TaW sample. (a) Cross section dictionary, D, with ^{181}Ta isotope and Tungsten W in natural abundances in units of $\mathrm{cm}^2/\mathrm{mol}$. (b) Effective open beam (yellow dashed), Ω_z measurement $\mathbf{y}_{\mathrm{sz}}$ (blue), fit of $\mathbf{y}_{\mathrm{sz}}$ (blue dashed), effective background (red dashed).

TABLE III
NUISANCE PARAMETER VALUES FOR THE TaW SAMPLE

Quantity	Estimates
$\begin{bmatrix} \text{isotopes} \\ \hat{\mathbf{z}}^\top\,[\mathrm{mmol/cm^2}] \end{bmatrix}$	$\begin{bmatrix} ^{181}\mathrm{Ta} & \mathrm{W} \\ 20.59 & 21.68 \end{bmatrix}$
$\alpha_1,\ \alpha_2$	$0.483,\ 0.685$
$\theta^\top$	$[29.9 \quad -56.1 \quad 5.39]$

Fig. 12(a) shows the cross section dictionary, D, used for this experiment. Since tantalum in natural abundance consists of practically 100 % of the ^{181}Ta isotope, we use this isotope for the cross section dictionary. In contrast, natural tungsten consists of several isotopes, so for its cross section we use a proportionally weighted sum of the cross section of its isotopes, ^{182}W, ^{183}W, ^{184}W, and ^{186}W.

Fig. 12(b) shows the plots corresponding to the nuisance parameter estimation of (24). Note that (compared to Fig. 6), the fit of $\mathbf{y}_{\mathrm{s0}}$ is not shown since there is no Ω_0 region. Nevertheless, the optimization seems to result in a good fit and plausible spectra of the effective flux and background.

Table III shows the numerical values of the nuisance parameters. Note that the α_2 parameter is relatively different from 1, indicating that the effects of the sample on the background are important to model.

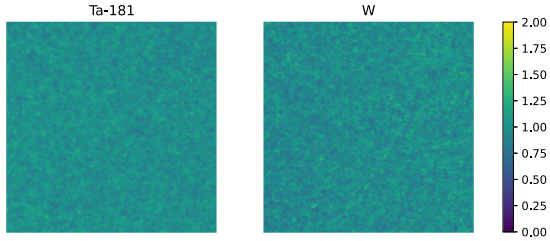

Fig. 13. Normalized areal density estimates, $\hat{Z}\,\mathrm{diag}(\hat{\mathbf{z}})^{-1}$, for the TaW sample [unitless].

TABLE IV
MEAN AND STANDARD DEVIATION OF AREAL DENSITIES AND THICKNESSES VS. GROUND TRUTH THICKNESSES OF THE TaW SAMPLE

Quantity \ Isotopes	^{181}Ta	W
Areal Density Estimate $[\frac{\mathrm{mmol}}{\mathrm{cm}^2}]$	20.56 ± 1.59	21.11 ± 2.09
Ground Truth Thickness [cm]	0.242	0.175
Estimated Thickness [cm]	$\mathbf{0.223 \pm 0.017}$	$\mathbf{0.197 \pm 0.020}$

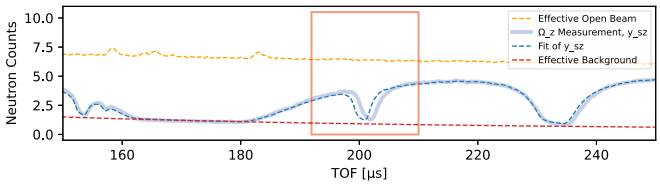

Fig. 14. Nuisance parameter estimation fits for the TaW sample. The plot shows a cropped TOF region where the red box indicates likely error in the tabulated energy of a Ta resonance. .

Fig. 13 shows the areal density estimates, $\hat{Z}\,\mathrm{diag}(\mathbf{z})^{-1}$. We observe that, apart from some noise, the estimates are visually relatively constant as is expected from a spatially constant sample. The noise level appears to be similar to the simulated data of Section VIII-B, however, it seems to be more spatially correlated, indicating possible detector cross talk.

Since the TaW sample matches the idealized example from Section II we can use (2) and the areal density estimates, to make a thickness estimate for each of the plates. Table IV shows the mean and standard deviation computed from the areal density estimates, $\hat{Z}$, the resulting estimated thicknesses and the ground truth thicknesses of the plates. The estimated thicknesses are relatively close to the actual thicknesses with an error of less than 13%.

We believe that the slight inaccuracies in Table III may be primarily inaccuracies in the assumed values of R and D. We rely on previous measurements by [46] for the parameters of R, which may not be sufficiently accurate. In addition, for the cross sections, D, we use tabulated data from ENDF/B-VIII.0 [44], which is empirically compiled and may not be sufficiently accurate for our experiment. In order to support our conjecture, Fig. 14 highlights a region (red box) in the spectrum where there are likely errors in D. In this region, the fitted resonance energy (blue dashed) in ^{181}Ta near 200 μs has a slightly lower TOF than the measured resonance (blue solid). This type of mismatch can significantly affect the density estimates. There are likely other

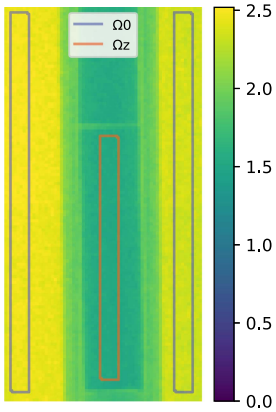

Fig. 15. TOF integrated measurement ratio, $\frac{Y_s^{(k)}\mathbb{1}}{Y_o\mathbb{1}}$, of the fuel pellet sample of a single view. Open beam region, Ω_0 (blue), and uniformly dense region, Ω_z (red).

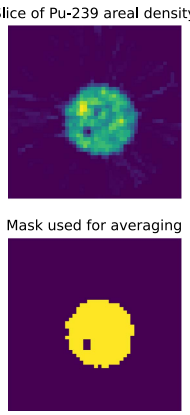

Fig. 16. Slice of the volumetric density, $\hat{X}$, of ^{239}Pu and corresponding mask generated through thresholding and used to determine average volumetric densities, $\hat{\mathbf{x}}$.

errors in the cross sections, which may however not be as obvious to spot as this one.

D. 3D Reconstruction From Experimental Data

In this experiment we demonstrate the tomographic reconstruction extension that is described in Section VI on measured experimental data of a transmutation nuclear fuel pellet sample. We will also compute average volumetric mass densities and validate them through independent mass spectroscopy measurements.

Fig. 15 shows the TOF integrated measurement ratio, $\frac{Y_s^{(k)}\mathbb{1}}{Y_o\mathbb{1}}$, of a single rotational view. The cylindrical nuclear fuel pellet is surrounded by a double wall steel cladding. We choose the regions surrounding the sample as the Ω_0 region and a thin axial region the center of the sample as the Ω_z region in the radiograph selected for the nuisance parameter estimation.

Fig. 17 shows the cross section dictionary, D. We assume that the sample contains the resonant isotopes ^{237}Np, ^{238}U, ^{239}Pu, ^{240}Pu, ^{241}Am. We also assume there are non-resonant materials such as for example Zr in the fuel and steel in the double wall

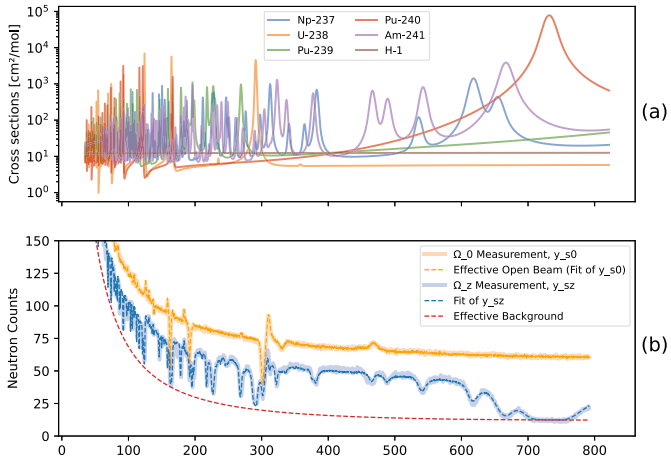

Fig. 17. Nuisance parameter estimation fits of the fuel pellet sample. (a) Cross section dictionary, D, with ^{237}Np, ^{238}U, ^{239}Pu, ^{240}Pu, ^{241}Am, and ^{1}H isotopes in units of $\mathrm{cm}^2/\mathrm{mol}$. (b) Ω_0 measurement $\mathbf{y}_{s0}$ (yellow), effective open beam (yellow dashed), Ω_z measurement $\mathbf{y}_{sz}$ (blue), fit of $\mathbf{y}_{sz}$ (blue dashed), effective background (red dashed).

TABLE V
NUISANCE PARAMETER VALUES FOR THE FUEL PELLET SAMPLE

Quantity	Estimates
$\begin{bmatrix}\text{isotopes}\\ \hat{\mathbf{z}}^\top\,[\mathrm{mmol/cm^2}]\end{bmatrix}$	$\begin{bmatrix}^{237}\mathrm{Np} & ^{238}\mathrm{U} & ^{239}\mathrm{Pu} & ^{240}\mathrm{Pu} & ^{241}\mathrm{Am} & ^{1}\mathrm{H}\\ 0.57 & 12.9 & 2.89 & 0.738 & 0.584 & 23.8\end{bmatrix}$
$\hat{\alpha}_1,\ \hat{\alpha}_2$	$2.39,\ 1.02$
$\hat{\theta}^\top$	$[112.3 \quad -39.0 \quad 15.1]$

cladding. For this reason, the cross section dictionary, D, not only includes the resonant isotopic cross sections but also the mostly constant ^{1}H (hydrogen) cross section. The reconstructed areal density associated with ^{1}H is interpreted as hydrogen-equivalent areal density, regardless whether the sample contains any hydrogen.

The sample is imaged at $N_r = 101$ different rotational views. The $N_A = 2440$ TOF bins span an interval from 47.6 μs up to 791.7 μs which corresponds to an energy range of 249.8 eV down to 0.902 eV, respectively. We use a cropped region of the detector of $N_p = 256 \times 512$ pixels. We applied a 4× binning because the measurements suffer from severe defects such as many malfunctioning detector rows and columns. We understand that in general binning may not be the best way to remove such defects, however, for simplicity sake we deemed this procedure appropriate.

Fig. 17(b) shows the fits resulting from the nuisance parameter estimation of one single view. The good fits of the respective measurements indicate successful estimation of the parameters. Table V lists the estimated parameters.

Fig. 18 shows the normalized areal density reconstruction, $\hat{Z}^{(k)}\,\mathrm{diag}(\hat{\mathbf{z}})^{-1}$, of a single view from the material decomposition. Each of the resonant isotopes, ^{237}Np, ^{238}U, ^{239}Pu, ^{240}Pu, ^{241}Am, clearly resolves the cylindrical fuel pellet while the ^{1}H equivalent density is mostly concentrated in the cladding.

Fig. 19 shows a single axial slice of the normalized volumetric density reconstruction, $\hat{X}\,\mathrm{diag}(\hat{\mathbf{x}})^{-1}$, from (33). We computed the vector $\hat{\mathbf{x}} \in \mathbb{R}^{N_m}$ as the average estimated volumetric density

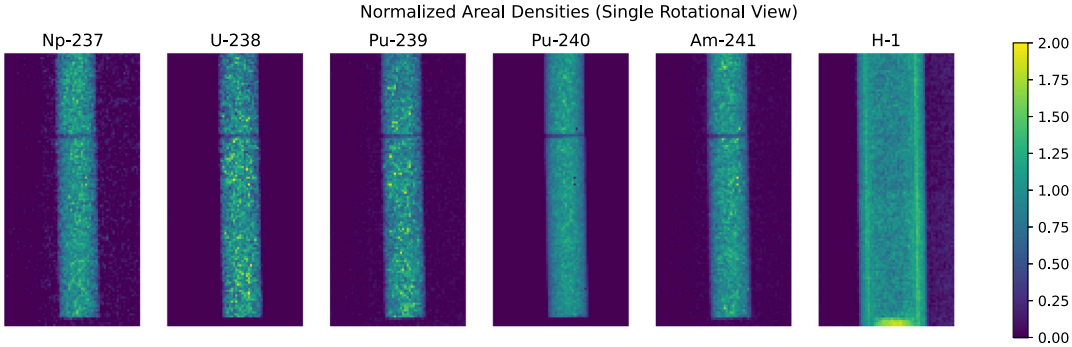

Fig. 18. Single view of the normalized areal density results for the fuel pellet sample, $\hat{Z}^{(k)}\,\mathrm{diag}(\hat{\mathbf{z}})^{-1}$ [unitless].

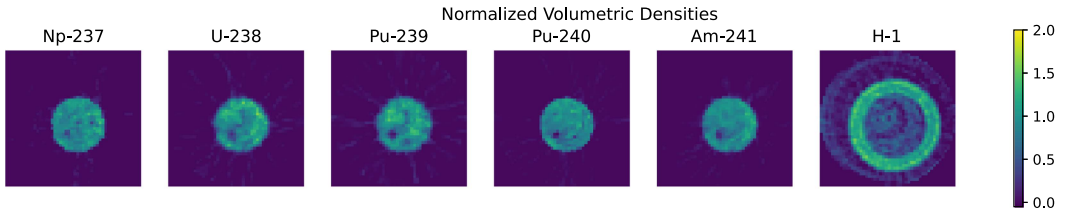

Fig. 19. Slice of the normalized volumetric density results for the fuel pellet sample, $\hat{X}\,\mathrm{diag}(\hat{\mathbf{x}})^{-1}$, [unitless]. (^{1}H is normalized as $\hat{X}_{*,i}/(3\hat{\mathbf{x}}_i)$) .

TABLE VI
AVERAGE VALUES OF VOLUMETRIC DENSITIES, $\hat{\mathbf{x}}$, OF THE FUEL PELLET SAMPLE IN UNITS OF $[\mathrm{mmol/cm^3}]$

Quantity	Estimates					
$\begin{bmatrix}\text{isotopes}\\ \hat{\mathbf{x}}^\top\end{bmatrix}$	$\begin{bmatrix}^{237}\mathrm{Np}\\ 1.394\end{bmatrix}$	$\begin{bmatrix}^{238}\mathrm{U}\\ 37.87\end{bmatrix}$	$\begin{bmatrix}^{239}\mathrm{Pu}\\ 8.369\end{bmatrix}$	$\begin{bmatrix}^{240}\mathrm{Pu}\\ 1.814\end{bmatrix}$	$\begin{bmatrix}^{241}\mathrm{Am}\\ 1.409\end{bmatrix}$	$\begin{bmatrix}^{1}\mathrm{H}\\ 55.7\end{bmatrix}$

TABLE VII
MASS DENSITY ESTIMATES THE FUEL PELLET SAMPLE COMPARED TO MASS SPECTROMETRY [36] (GROUND TRUTH) IN UNITS OF $\mathrm{g/cm^3}$

Mass Density \ Isotopes	$^{237}\mathrm{Np}$	$^{238}\mathrm{U}$	$^{239}\mathrm{Pu}$	$^{240}\mathrm{Pu}$	$^{241}\mathrm{Am}$
Ground Truth	0.34	9.01	2.34	0.37	0.32
Estimated	**0.331**	**9.014**	**2.000**	**0.435**	**0.340**

in the mask shown in Fig. 16. The the values of $\hat{\mathbf{x}}$ are shown in Table VI. In the displayed slice the clear separation between fuel and cladding is visible. Also, there is a void visible in the 7-o'clock position in all resonant isotope maps, indicating what is probably a void in the sample.

Finally, Table VII shows the average reconstructed mass density estimates, $\hat{\boldsymbol{\rho}}^{[\mathrm{g/cm^3}]}$, computed from the volumetric densities, $\hat{\mathbf{x}}^{[\mathrm{mol/cm^3}]}$ and the relationship in (3). The table also lists the values of ground truth measurements obtained using mass spectroscopy. Note that the reconstructed estimates are very close to the ground truth values which provides strong experimental validation of our method.

IX. CONCLUSION

We present a novel method for both 2D and 3D reconstruction of material areal and volumetric density from TOF neutron images. Our method, TRINIDI, accounts for a number of important measurement effects including spatially varying background, non-uniform flux, finite pulse duration, and Poisson counting noise. Especially, when including the finite pulse duration in the forward model, the problem cannot be linearized in the same fashion that is common with Beer-Law attenuation models. TRINIDI is based on a 2-step process in which we first estimate nuisance parameters associated with background and flux, and we then reconstruct the unknown isotopic areal density. For the 3D case, we then perform tomographic reconstruction of the views to form a 3D volumetric density estimate. Both our simulated and experimental results indicate that TRINIDI can reconstruct quantitatively accurate estimates in both 2D and 3D. Notably, comparisons of our 3D material decomposed reconstructions for nuclear fuel pellets are accurate when compared to mass spectroscopy measurements.

APPENDIX A
RESOLUTION FUNCTION

The resolution operator, R, models the uncertainty of emission time of the neutrons given their known neutron energy. Equivalently, it models the conditional probability of TOA's given the neutron's TOF's, stated more precisely in (4). Since the pulse shape changes with every neutron energy, we choose to approximate the resolution operator using a weighted sum of K convolution operations, so that

$$R = \sum_{k=0}^{K-1} R^k W^k. \tag{47}$$

The R^k matrix corresponds to the convolution operation with kernel $\mathbf{r}^k$, which in turn corresponds to the pulse shape at the TOF bin with index $\lfloor k\frac{N_\mathrm{F}-1}{K-1}\rfloor$. The W^k matrices are diagonal

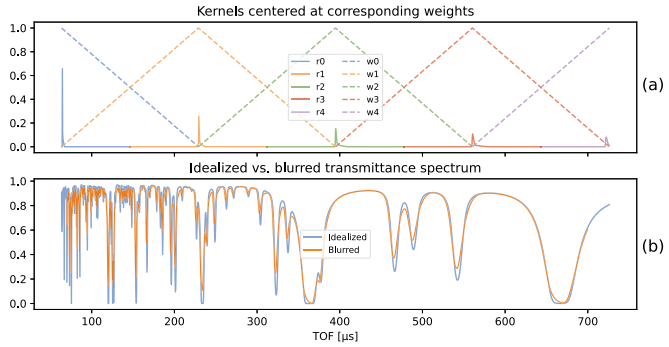

Fig. 20. Illustration of resolution function with $K = 5$ components applied to transmission spectrum. (a) Dashed lines: $\mathbf{w}^k$ weights. Solid lines: $\mathbf{r}^k$ blurring kernels centered at TOF where they are most active. (b) Blue line: non-blurred transmission spectrum. Orange line: blurred transmission spectrum using the kernels above.

weighting matrices with diagonals $\mathbf{w}^k$ which blend together the blurring operators, R^k.

Fig. 20 illustrates the application of the resolution operator with $K = 5$ components in a typical scenario. In Fig. 20(a) the dashed lines are the diagonals, $\mathbf{w}^k$ and the solid lines are the corresponding kernels, $\mathbf{r}^k$ centered at the TOF where they are most active. The blue line in Fig. 20(b) shows a typical non-blurred transmission spectrum, $\exp(-\mathbf{z}^\top D)$. The orange line shows the corresponding blurred transmission spectrum, $\exp(-\mathbf{z}^\top D)R$. Note that the blurring is weaker in the low-TOF region and stronger in the high-TOF region and that black resonances in the non-blurred signal are mostly not opaque after the blurring.

Next we show that $\mathbb{1}^\top R = \mathbb{1}^\top$. First, we select the weights so every TOA bin they sum to 1, i.e.

$$\sum_{k=0}^{K-1} W^k = I\,. \tag{48}$$

Second, we assume that $\sum_j \mathbf{r}_j^k = 1$ so that every emitted neutron is measured as some TOA bin. As explained in Section III this is achieved by choosing the number of rows of R^k to be sufficiently large so that

$$(\forall k)\ \sum_i R_{i,j}^k = \sum_i \mathbf{r}_{j-i}^k = \sum_i \mathbf{r}_j^k = 1$$

so we have that

$$(\forall k)\ \mathbb{1}^\top R^k = \mathbb{1}^\top\,. \tag{49}$$

Finally, using (47), (48), and (49) we see that

$$\begin{aligned}\mathbb{1}^\top R &= \mathbb{1}^\top \left(\sum_{k=0}^{K-1} R^k W^k\right) = \sum_{k=0}^{K-1} \left(\mathbb{1}^\top R^k\right) W^k \\ &= \sum_{k=0}^{K-1} \mathbb{1}^\top W^k = \mathbb{1}^\top \left(\sum_{k=0}^{K-1} W^k\right) = \mathbb{1}^\top I = \mathbb{1}^\top\,. \end{aligned} \tag{50}$$

Appendix B
Spectral Basis Matrix of the Background

In this work, we choose the background basis to be

$$P_{n,k} = \frac{1}{a_n} \left(\log\left[k\Delta + k_0\right]\right)^n\,, \tag{51}$$

where $a_n = \sqrt{\sum_{k=0}^{N_\mathrm{A}-1} [(\log[k\Delta + k_0])^n]^2}$ scales the rows of P so they have unit norm and $0 \le n < N_\mathrm{b}$, $0 \le k < N_\mathrm{A}$, and we have found that scalar $\Delta = \frac{\mathrm{e}^1 - \mathrm{e}^{-1}}{N_\mathrm{A}-1}$ and the offset $k_0 = \mathrm{e}^{-1}$ work well across a range of cases.

References

[1] J. Banhart et al., "X-ray and neutron imaging–complementary techniques for materials science and engineering," *Int. J. Mater. Res.*, vol. 101, no. 9, pp. 1069–1079, 2010.

[2] I. S. Anderson, R. L. McGreevy, and H. Z. Bilheux, "Neutron imaging and applications," *Springer Sci. Bus. Media*, vol. 200, no. 2209, 2009.

[3] L. G. Tumlinson, H. Liu, W. K. Silk, and J. W. Hopmans, "Thermal neutron computed tomography of soil water and plant roots," *Soil Sci. Soc. Amer. J.*, vol. 72, no. 5, pp. 1234–1242, 2008.

[4] M. W. Malone et al., "In vivo observation of tree drought response with low-field NMR and neutron imaging," *Front. Plant Sci.*, vol. 7, 2016, Art. no. 564.

[5] P. Vontobel, E. H. Lehmann, R. Hassanein, and G. Frei, "Neutron tomography: Method and applications," *Physica B: Condens. Matter*, vol. 385, pp. 475–480, 2006.

[6] N. Kardjilov, I. Manke, R. Woracek, A. Hilger, and J. Banhart, "Advances in neutron imaging," *Mater. Today*, vol. 21, no. 6, pp. 652–672, 2018.

[7] R. F. Ziesche et al., "4D imaging of lithium-batteries using correlative neutron and X-ray tomography with a virtual unrolling technique," *Nature Commun.*, vol. 11, no. 1, pp. 1–11, 2020.

[8] A. Tengattini et al., "Next-grenoble, the neutron and X-ray tomograph in grenoble," *Nucl. Instrum. Methods Phys. Res., A*, vol. 968, 2020, Art. no. 163939.

[9] J. W. G. Thomason, "The ISIS spallation neutron and muon source–the first thirty-three years," *Nucl. Instrum. Methods Phys. Res., A*, vol. 917, pp. 61–67, 2019.

[10] P. W. Lisowski and K. F. Schoenberg, "The los alamos neutron science center," *Nucl. Instrum. Methods Phys. Res., A*, vol. 562, no. 2, pp. 910–914, 2006.

[11] H. Z. Bilheux et al., "Neutron imaging at the oak ridge national laboratory: Application to biological research," in *Proc. IEEE Biomed. Sci. Eng. Conf.*, 2014, pp. 1–4.

[12] Y. Ikeda, "Current status of 1 MW pulse spallation neutron source (JSNS) of J-PARC," *J. Nucl. Mater.*, vol. 343, no. 1-3, pp. 7–13, 2005.

[13] E. H. Lehmann et al., "The energy-selective option in neutron imaging," *Nucl. Instrum. Methods Phys. Res., A*, vol. 603, no. 3, pp. 429–438, 2009.

[14] A. Hilger et al., "Neutron guide optimisation for a time-of-flight neutron imaging instrument at the European spallation source," *Opt. Exp.*, vol. 23, no. 1, pp. 301–311, Jan. 2015.

[15] W. Kockelmann, G. Frei, E. H. Lehmann, P. Vontobel, and J. R. Santisteban, "Energy-selective neutron transmission imaging at a pulsed source," *Nucl. Instrum. Methods Phys. Res., A*, vol. 578, no. 2, pp. 421–434, 2007.

[16] P. Schillebeeckx, B. Becker, H. Harada, and S. Kopecky, "Neutron resonance spectroscopy for the characterisation of materials and objects," Joint Research Centre European Commission, Luxembourg, 2014.

[17] H. Sato, T. Kamiyama, and Y. Kiyanagi, "Pulsed neutron imaging using resonance transmission spectroscopy," *Nucl. Instrum. Methods Phys. Res., A*, vol. 605, no. 1-2, pp. 36–39, 2009.

[18] A. S. Tremsin, W. Kockelmann, D. E. Pooley, and W. B. Feller, "Spatially resolved remote measurement of temperature by neutron resonance absorption," *Nucl. Instrum. Methods Phys. Res., A*, vol. 803, pp. 15–23, 2015.

[19] K. V. Tran et al., "Spectral neutron tomography," *Mater. Today Adv.*, vol. 9, 2021, Art. no. 100132.

[20] R. Woracek et al., "Neutron bragg-edge-imaging for strain mapping under in situ tensile loading," *J. Appl. Phys.*, vol. 109, no. 9, 2011, Art. no. 0 93506.

[21] G. Breit and E. Wigner, "Capture of slow neutrons," *Phys. Rev.*, vol. 49, no. 7, pp. 519–531, 1936.

[22] M. Mocko, G. Muhrer, and F. Tovesson, "Advantages and limitations of nuclear physics experiments at an ISIS-class spallation neutron source," *Nucl. Instrum. Methods Phys. Res., A*, vol. 589, no. 3, pp. 455–464, 2008.
[23] T. Ino et al., "Measurement of neutron beam characteristics at the manuel lujan jr. neutron scattering center," *Nucl. Instrum. Methods Phys. Res., A*, vol. 525, no. 3, pp. 496–510, 2004.
[24] A. S. Tremsin et al., "Non-destructive studies of fuel pellets by neutron resonance absorption radiography and thermal neutron radiography," *J. Nucl. Mater.*, vol. 440, no. 1-3, pp. 633–646, 2013.
[25] H. Postma and P. Schillebeeckx, "Neutron resonance capture and transmission analysis," *Encyclopedia Anal. Chem.*, vol. 10, no. 9780470027318, 2009, Art. no. a9070.
[26] P. Schillebeeckx et al., "Determination of resonance parameters and their covariances from neutron induced reaction cross section data," *Nucl. Data Sheets*, vol. 113, no. 12, pp. 3054–3100, 2012.
[27] F. Ma et al., "Non-destructive analysis of samples with a complex geometry by NRTA," *J. Anal. At. Spectrometry*, vol. 35, no. 3, pp. 478–488, 2020.
[28] H. Hasemi et al., "Evaluation of nuclide density by neutron resonance transmission at the noboru instrument in J-PARC/MLF," *Nucl. Instrum. Methods Phys. Res., A*, vol. 773, pp. 137–149, 2015.
[29] N. M. Larson, "Updated users' guide for SAMMY multilevel r-matrix fits to neutron data using bayes' equation," *Oak Ridge Nat. Lab*., Oak Ridge, TN, USA, Tech. Rep. ORNL/TM-9179/R4, 2008. [Online]. Available: https://www.ornl.gov/onramp/sammy
[30] C. De Saint Jean, B. Habert, O. Litaize, G. Noguere, and C. Suteau, "Status of CONRAD, a nuclear reaction analysis tool," in *Proc. Int. Conf. Nucl. Data Sci. Technol.*, 2007, pp. 251–254.
[31] M. C. Moxon, "REFIT: A least quare fitting program for resonance analysis of neutron transmission data," Commission of the European Communities (CEC), Tech. Rep., 1979, pp. 644–674.
[32] A. S. Tremsin, J. Rakovan, T. Shinohara, W. Kockelmann, A. S. Losko, and S. C. Vogel, "Non-destructive study of bulk crystallinity and elemental composition of natural gold single crystal samples by energy-resolved neutron imaging," *Sci. Rep.*, vol. 7, no. 1, pp. 1–9, 2017.
[33] T. Kamiyama, H. Sato, N. Miyamoto, H. Iwasa, Y. Kiyanagi, and S. Ikeda, "Energy sliced neutron tomography using neutron resonance absorption spectrometer," *Nucl. Instrum. Methods Phys. Res., A*, vol. 600, no. 1, pp. 107–110, 2009.
[34] G. Festa et al., "Neutron resonance transmission imaging for 3D elemental mapping at the isis spallation neutron source," *J. Anal. At. Spectrometry*, vol. 30, no. 3, pp. 745–750, 2015.
[35] A. S. Losko and S. C. Vogel, "3D isotope density measurements by energy-resolved neutron imaging," *Sci. Rep.*, vol. 12, no. 1, 2022, Art. no. 6648.
[36] S. C. Vogel, D. D. Byler, E. Kardoulaki, and K. J. Mcclellan, "Neutron resonance spectroscopy applications for nuclear fuel characterization," Los Alamos Nat. Lab., Los Alamos, NM, USA, Tech. Rep. LA-UR–18-248742018.
[37] T. Balke, A. M. Long, S. C. Vogel, B. Wohlberg, and C. A. Bouman, "Hyperspectral neutron CT with material decomposition," in *Proc. IEEE Int. Conf. Image Process.*, 2021, pp. 3482–3486.
[38] D. B. Syme, "The black and white filter method for background determination in neutron time-of-flight spectrometry," *Nucl. Instrum. Methods Phys. Res.*, vol. 198, no. 2-3, pp. 357–364, 1982.
[39] T. Balke, A. M. Long, S. C. Vogel, B. Wohlberg, and C. A. Bouman, "Time-of-flight resonance imaging with neutrons for isotopic density inference (TRINIDI)," 2023. [Online]. Available: https://github.com/lanl/trinidi
[40] G. T. Buzzard, S. H. Chan, S. Sreehari, and C. A. Bouman, "Plug-and-play unplugged: Optimization-free reconstruction using consensus equilibrium," *SIAM J. Imag. Sci.*, vol. 11, no. 3, pp. 2001–2020, 2018.
[41] T. Balke et al., "Separable models for cone-beam MBIR reconstruction," *Electron. Imag.*, vol. 2018, no. 15, p. 181-1–1817, 2018.
[42] S. Majee, T. Balke, C. A. J. Kemp, G. T. Buzzard, and C. A. Bouman, "Multi-slice fusion for sparse-view and limited-angle 4D CT reconstruction," *IEEE Trans. Comput. Imag.*, vol. 7, pp. 448–462, 2021.
[43] S. V. Venkatakrishnan, C. A. Bouman, and B. Wohlberg, "Plug-and-play priors for model based reconstruction," in *Proc. IEEE Glob. Conf. Signal Inf. Process.*, 2013, pp. 945–948.
[44] J. L. Conlin, W. Haeck, D. Neudecker, D. Kent Parsons, and M. C. White, "Release of endf/b-viii. 0-based ace data files," Los Alamos Nat. Lab, Los Alamos, NM, USA, Tech. Rep LA-UR-18-24034, 2018.
[45] A. S. Tremsin et al., "Detection efficiency, spatial and timing resolution of thermal and cold neutron counting MCP detectors," *Nucl. Instrum. Methods Phys. Res., A*, vol. 604, no. 1-2, pp. 140–143, 2009.
[46] J. E. Lynn, W. J. Trela, and K. Meggers, "Neutron doppler broadening studies of tantalum and tungsten metal," *Nucl. Instruments Methods Phys. Res. Sect. B: Beam Interact. Mater. At.*, vol. 192, no. 3, pp. 318–330, 2002.
[47] T. Balke et al., "Super-voxel model based iterative reconstruction (SVMBIR)," 2023. [Online]. Available: https://github.com/cabouman/svmbir
[48] T. Balke et al., "Scientific computational imaging code (SCICO)," *J. Open Source Softw.*, vol. 7, no. 78, 2022, Art. no. 4722.

Thilo Balke (Member, IEEE) received the B.Sc. degree in electrical engineering and information technology from Ruhr-University Bochum, Bochum, Germany, in 2014, and the Ph.D. degree in electrical engineering and computer science with Purdue University, West Lafayette, IN, USA, in 2023. From 2019 to 2023, he was a Graduate Research Assistant with the Theoretical Division, Los Alamos National Laboratory, Los Alamos, NM, USA. Since 2023, he has been a Research Engineer with Samsung Research America, Plano, TX, USA. His research interests include computational imaging, inverse problems, high-performance computing, machine learning, and stochastic image modeling.

Alexander M. Long is currently an early career staff Scientist of LANL with a Ph.D. in nuclear physics from the University of Notre Dame. As the current instrument scientist for flight path five and flight path 11 with the Los Alamos Neutron Science Center (LANSCE). His main research interests include developing and implementing advanced neutron imaging techniques, such as energy resolved neutron imaging, neutron resonance imaging, and Bragg edge imaging, to explore new and novel materials for the nuclear energy community.

Sven C. Vogel received the Ph.D. (Dr. rer. nat.) degree in physics in 2000 and holds diplomas (equivalent to U.S. master degree) in physics and mineralogy from Christian-Albrecht University, Kiel, Germany. In 2001, he came to Los Alamos National Laboratory as a Postdoc with the Materials Science and Technology Division and became staff in 2002 with the Los Alamos Neutron Science Center. He has authored and co-authored more than 400 publications with more than 10 000 citations per Google Scholar and contributed to chapters for several textbooks. His research interests include deformation mechanisms and phase transformations in metals, alloys, and rocks, in-situ neutron and synchrotron diffraction loading measurements, texture measurements, phase transformation textures, Bragg-edge and resonance absorption neutron transmission and imaging, and radiography & tomography. He has operated the neutron diffractometer HIPPO at LANSCE in 2002, with more than 400 user proposals carried out. He was the recipient of the Award of Excellence for a significant contribution to the stockpile stewardship in 2005 and 2009 and the LANSCE User Facility Director's Award 2009. He has also been a Faculty Adjunct with the New Mexico Institute of Mining and Technology since 2011.

Brendt Wohlberg (Fellow, IEEE) received the B.Sc. (Hons.) degree in applied mathematics, and the M.Sc. (applied science) and Ph.D. degrees in electrical engineering from the University of Cape Town, Cape Town, South Africa. He is currently a Staff Scientist with Theoretical Division, Los Alamos National Laboratory. He was the Chair of the Computational Imaging Special Interest Group (now the Computational Imaging Technical Committee) of the IEEE Signal Processing Society and was an Editor-in-Chief of IEEE TRANSACTIONS ON COMPUTATIONAL IMAGING. He is currently an Editor-in-Chief of the IEEE OPEN JOURNAL OF SIGNAL PROCESSING.

Charles A. Bouman (Life Fellow, IEEE) received the B.S.E.E. degree from the University of Pennsylvania, Philadelphia, PA, USA, the M.S. degree from the University of California at Berkeley, Berkeley, CA, USA, and the Ph.D. degree from Princeton University, Princeton, NJ, USA. He is currently the Showalter Professor of Electrical and Computer Engineering and Biomedical Engineering, Purdue University, West Lafayette, IN, USA. He is a Member of the National Academy of Inventors, a Fellow of AIMBE, IS&T, and SPIE. He was the recipient of the 2021 IEEE Signal Processing Society, Claude Shannon-Harry Nyquist Technical Achievement Award. He was the IEEE Signal Processing Society's Vice President of Technical Directions as well as the Editor-in-Chief of IEEE TRANSACTIONS ON IMAGE PROCESSING.